Study of ATLAS sensitivity to the single top Wt-channel cross section

Master's Thesis

Maria Inês A. J. Ochoa de Castro
`inesochoa@gmail.com`

Orientador: Professor Doutor António Joaquim Onofre de A. R. Gonçalves
Co-Orientador: Professor Doutor João Carlos Lopes Carvalho

Coimbra, 2010

ii

Resumo

Realizou-se o estudo da sensibilidade da experiência ATLAS, do LHC, à medida da secção eficaz do canal *Wt* de *single top*. Para tal, utilizou-se a simulação completa do detector (FullSim) a uma energia de centro de massa de $\sqrt{s} = 7$ TeV. Os acontecimentos de sinal e de alguns processos de fundo foram gerados pelo gerador MC@NLO. Outros processos de fundo foram gerados através do gerador ALPGEN (ex.: *W*+jactos) ou HERWIG. Foi desenvolvida uma análise sequencial e discriminante para distinguir o sinal e o fundo existentes, a uma luminosidade de 200 pb^{-1}. Com os resultados obtidos foi calculada a secção eficaz do canal *Wt* de *single top* e a respectiva incerteza estatística.

Abstract

The sensitivity of the ATLAS experiment, on the LHC, to the measurement of the single top Wt-channel cross section was studied. The full simulation (FullSim) of the detector was used at a centre-of-mass energy of $\sqrt{s} = 7$ TeV. Signal events and some background processes were generated using MC@NLO generator. Other background processes were generated using ALPGEN (for example W+jets) or HERWIG. A sequential and a discriminant analysis were developed for a luminosity of $200\,\mathrm{pb}^{-1}$ to distinguish between signal and background events. From the results obtained, the cross section of the Wt-channel was calculated as well as its statistical uncertainty.

Acknowledgements

First of all, I would like to express my gratitude to my supervisors, Professors António Onofre and João Carvalho for their support, guidance and expertise. For the precious help and patience I am grateful to Nuno Castro, Filipe Veloso and Miguel Fiolhais, with whom I learned so much. I also thank Professor Orlando Oliveira and Rita Monteiro for the clarifications given in the Theoretical Framework chapter of this thesis.

I deeply thank my friends and colleagues Susana Santos and Nuno Ferreira for their friendship and companionship, supporting me in every way. To all my other colleagues during these years, thank you for making it such a great experience to study physics in Coimbra. I also thank my long time friends Rita, Cristina, Filipa and my fellow musicians for every moment I spent thinking about everything else but work.

I owe my deepest gratitude to my parents, Constança and the rest of my family for the love and support.

Last but not least, I thank João Nuno for all that goes without saying and for such a surprising and unexpected turn of events.

Contents

List of Figures

List of Tables

Chapter 1

Introduction

The Large Hadron Collider at CERN has started its operation in the year 2009 and is currently in the first physics run at a centre of mass energy of 7 TeV. Given its expected nominal centre of mass energy of $\sqrt{s} = 14$ TeV and an integrated luminosity of 10 fb^{-1} per year and per experiment (in the low luminosity phase), the LHC will be a top quark factory. Since the amount of statistics available will be unprecedently large, the determination of the top quark properties with high precision will be possible.

The top quark can be produced in the LHC by two main mechanisms: pair production ($t\bar{t}$), via the strong interaction, and single top production, via the electroweak interaction (t-channel, s-channel, Wt-channel), which has a smaller cross section. Pair production was the process by which the quark top was first observed, at Fermilab, by the CDF and D0 experiments in 1995 [9, 10]. Recently, in 2009, the first observation of single top quark production (t + s channels) was reported by both experiments [20, 21]. In these experiments, the low statistics didn't allow measurements besides the cross section in the single top channels. However, in the pair production process, the top quark mass was measured with a precision of $\sim 1\%$ [11].

Presently, the LHC has already produced several millions of events at a centre of mass energy of $\sqrt{s} = 7$ TeV, corresponding to an integrated luminosity of $\mathcal{L} \simeq 148$ nb^{-1} recorded by ATLAS (by July 2010). The analysis in this thesis was done using simulated collisions at $\sqrt{s} = 7$ TeV and for a low luminosity run of 200 pb^{-1}.

The semileptonic Wt-channel single top quark production was the process studied in the present thesis. Due to the energy of the Tevatron collisions and the luminosity of the recorded data, this channel hasn't been experimentally observed yet. At the LHC, the Wt-channel has a larger cross section due to the higher centre-of-mass energy which increases the gluon interactions, conditions which will allow its observation and study.

1

To eliminate as much background contamination as possible from signal events, a sequential and a discriminant analysis were developed. After the analysis, a value for the cross section of the signal process was determined, with a corresponding statistical uncertainty.

This thesis is organized as follows. The Standard Model and the top quark are introduced in the second chapter, as well as the top quark properties and its production mechanisms. The LHC and the ATLAS experiment will then be presented and described in chapter 3. In chapter 4 the generation and simulation of events used in the analysis are discussed. Then, the description of the analysis itself, both the sequential and the discriminant, is done in chapter 5. The result for the value of the cross section is presented on the sixth chapter. Finally, chapter 7 is dedicated to the conclusions of this study.

Chapter 2

Theoretical Framework

"Whether or not the Large Hadron Collider reveals the long-awaited Higgs particle, it is likely to lead to discoveries that add to, or challenge, the standard model of particle physics." — John Ellis, in Nature 448 (2007) 297-301.

In the present chapter, the Standard Model of Particle Physics and other theoretical aspects relevant to this work are briefly introduced. The properties of the top quark and its production mechanisms at LHC are explained, in particular the single top quark production.

2.1 The Standard Model

The Standard Model (SM) is a gauge theory which incorporates the electromagnetic, weak and strong interactions. The Standard Model symmetry group is $SU(2)_L \times U(1)_Y \times SU(3)_c$, where the $SU(2)_L \times U(1)_Y$ and $SU(3)_c$ groups are associated with the electroweak and the strong force, respectively [1, 2, 3].

The SM postulates that all matter is composed of a few basic, point-like and structureless constituents: elementary particles. These are divided into two groups: fermions and bosons.

Fermions carry spin $1/2$ and obey the Pauli Exclusion Principle. They are classified into leptons and quarks. The known quarks are of six different flavours: up, down, charm, strange, top and bottom, formally described by flavour quantum numbers. The SM incorporates six leptons: the electron and the electron-neutrino, the muon and the muon-neutrino, the tau and the tau-neutrino. They carry electron, muon and tau quantum numbers. Each quark and each lepton has an associated antiparticle.

Quarks interact via the electromagnetic, weak and strong interactions, since they carry electric charge, weak isospin and an additional quantum number, the color charge, which

can be denoted generically as q_i, $i = 1, 2, 3$. Since color is not seen in Nature, we know these particles must be confined into color-neutral particles, the hadrons, which can be experimentally observed. To our knowledge, these colorless composite particles are divided into baryons (three quarks) and mesons (quark-antiquark systems).

All leptons experience the weak force, and the charged ones are also subject to the electromagnetic force. However, leptons do not take part in strong interactions, since they have no color charge.

The electromagnetic, weak and strong interactions between elementary particles can be described through the exchange of field quanta which are the force mediating particles. These particles carry spin 1 and are called gauge bosons. The electromagnetic force is mediated by the massless photon γ; the weak force by the massive $W^{\pm}$ ($m_W = 80.398 \pm 0.025 \text{GeV}/c^2$) and the Z^0 ($m_Z = 91.1876 \pm 0.0021 \text{GeV}/c^2$) [4]; the strong force by eight massless self-interacting gluons g that come in eight different color states.

Gravitation is not included in the framework of the SM but rather described by the theory of general relativity in a macroscopic scale. Due to the weakness of gravitation with respect to the other forces acting in elementary particle interactions, it is not further considered in the present thesis.

The SM Lagrangian is divided into two sectors associated with the electroweak interactions and the quantum chromodynamics:

$$\mathscr{L}_{SM} = \mathscr{L}_{electroweak} + \mathscr{L}_{QCD} \tag{2.1}$$

The electroweak interaction is the unification of the weak and the electromagnetic interactions, and is described by the Weinberg-Salam-Glashow model [5]. The hypercharge operator $\hat{Y}$ is the generator of $U(1)$ and the weak isospin operator $\hat{T}$ is the generator of $SU(2)$. The electric charge Q is related with the hypercharge Y and the third component of weak isospin T_3 according to $Q = \frac{1}{2}Y + T_3$.

The fermionic sector of SM is organized in three families with identical properties except for mass. The left-handed states of each family are grouped into weak-isospin doublets, while the corresponding right-handed states transform as singlets under $SU(2)_L$:

$$1^{st} \text{ family: } \begin{pmatrix} \nu_e \\ e^- \end{pmatrix}_L, e_R^-, \begin{pmatrix} u \\ d \end{pmatrix}_L, u_R, d_R$$

$$2^{nd} \text{ family: } \begin{pmatrix} \nu_\mu \\ \mu^- \end{pmatrix}_L, \mu_R^-, \begin{pmatrix} c \\ s \end{pmatrix}_L, c_R, s_R$$

$$3^{rd} \text{ family: } \begin{pmatrix} \nu_\tau \\ \tau^- \end{pmatrix}_L, \tau_R^-, \begin{pmatrix} t \\ b \end{pmatrix}_L, t_R, b_R$$

	Q	Y	T	T_3
u_L	2/3	1/3	1/2	1/2
d_L	-1/3	1/3	1/2	-1/2
u_R	2/3	4/3	0	0
d_R	-1/3	-2/3	0	0
v_L^e	0	-1	1/2	1/2
e_L^-	-1	-1	1/2	-1/2
e_R^-	-1	-2	0	0

Table 2.1: *Electroweak charges Q, Y and T, T_3 for quarks and leptons in the Standard Model.*

and their corresponding antiparticles.

The weak-isospin assignment for the doublet is: up-type quarks (u, c, t) and neutrinos carry $T_3 = +\frac{1}{2}$; down-type quarks (d, s, b), electron, muon and tau leptons have $T_3 = -\frac{1}{2}$. In the original SM the right-handed neutrino states are omitted, since neutrinos are assumed to be massless and the helicity and chirality states coincide. However, recent experimental evidence (see, for example, Ref. [6]) strongly indicates that neutrinos have mass, and the SM needs to be extended in this respect.

In Table 2.1 the quantum numbers Q, Y, T and T_3 of the Standard Model particles are shown.

The total Lagrangian density of the Electroweak Theory has contributions from the fermion kinetic and interactions terms, the gauge boson kinetic terms and the gauge boson self-interaction terms. It can be written as:

$$\mathscr{L}_{electroweak} = \mathscr{L}_{gauge} + \mathscr{L}_{fermions} + \mathscr{L}_{Higgs}. \tag{2.2}$$

The component associated with the gauge fields is given by:

$$\mathscr{L}_{gauge} = -\frac{1}{4}F_i^{\mu\nu}F_{\mu\nu}^i - \frac{1}{4}B^{\mu\nu}B_{\mu\nu}, \tag{2.3}$$

where

$$F_{\mu\nu}^i = \partial_\mu W_\nu^i - \partial_\nu W_\mu^i - g_2 \varepsilon^{ijk} W_\mu^j W_\nu^k, \tag{2.4}$$

$$B_{\mu\nu} = \partial_\mu B_\nu - \partial_\nu B_\mu, \tag{2.5}$$

with the gauge bosons W_μ^i, $i = 1, 2, 3$ and B_μ for the $SU(2)_L$ and $U(1)_Y$ groups. g_2 is the coupling constant for the $SU(2)$ and ε^{ijk} is an antisymmetric tensor. The Pauli matrices indices are represented by i, j, k while μ and ν are the Lorentz indices.

The fermionic part in 2.2 is defined as:

$$\mathscr{L}_{fermions} = \sum_{\psi_L} \bar{\psi}_L i\displaystyle{\not}D \psi_L + \sum_{\psi_R} \bar{\psi}_R i\displaystyle{\not}D \psi_R,$$

with the covariant derivative of the right and left handed components of the fermion fields $\Psi_{R,L}$ given by

$$\mathscr{D}_\mu \psi_R = \left(\partial_\mu + \frac{i}{2} g_1 Y B_\mu \right) \psi_R, \tag{2.6}$$

$$\mathscr{D}_\mu \psi_L = \left(\partial_\mu + \frac{i}{2} g_1 Y B_\mu + \frac{i}{2} g_2 \vec{\tau} \cdot \vec{W}_\mu \right) \psi_L, \tag{2.7}$$

where $\vec{\tau}$ are the Pauli matrices and g_1 is the gauge coupling constant for the $U(1)$ group.

Finally, the Higgs Lagrangian term contains the Higgs potential and the kinetic terms of the Higgs field, which has a non-zero vacuum expectation value that spontaneously breaks electroweak symmetry. The gauge boson and fermion masses are then generated in a gauge invariant way, in a mechanism that is referred to as the Higgs mechanism.

The boson fields resulting from the spontaneous symmetry breaking are, however, not the original fields $\mathbf{W}_\mu$ and B_μ but rather mixtures of those: the bosons $W_\mu^\pm = (W_\mu^1 \mp iW_\mu^2)/\sqrt{2}$, the Z^0 and the photon field A_μ, related by:

$$\begin{pmatrix} A_\mu \\ Z_\mu \end{pmatrix} = \begin{pmatrix} \cos\theta_W & \sin\theta_W \\ -\sin\theta_W & \cos\theta_W \end{pmatrix} \begin{pmatrix} B_\mu \\ W_\mu^3 \end{pmatrix}.$$

The mixing angle θ_W is the Weinberg angle and it is defined by the coupling constants as $g_2/g_1 = \tan\theta_W$.

Besides the electroweak interaction term, equation 2.1 also contains the gauge invariant Lagrangian for the strong interaction that describes the dynamics of quarks and gluons:

$$\mathscr{L}_{QCD} = \bar{\psi}_i \left(i\gamma^\mu (D_\mu)_{ij} - m\delta_{ij} \right) \psi_j - \frac{1}{4} G_{\mu\nu}^a G_a^{\mu\nu}$$

$$= \bar{\psi}_i \left(i\gamma^\mu \partial_\mu - m \right) \psi_i - g G_\mu^a \bar{\psi}_i \gamma^\mu T_{ij}^a \psi_j - \frac{1}{4} G_{\mu\nu}^a G_a^{\mu\nu}, \tag{2.8}$$

where T^a, $a = 1, ..., 8$, are the $SU(3)$ color generators and the matrix elements indices are represented by $i, j = 1, 2, 3$. The ψ_j are the spinors associated with each quark field of color j and mass m and $G_\mu^a(x)$ are the gluon fields. The Dirac matrices and coupling constant are given by γ^μ and g, respectively. The gluon field tensor is represented by:

$$G_{\mu\nu}^a = \partial_\mu G_\nu^a - \partial_\nu G_\mu^a - g f^{abc} G_\mu^b G_\mu^c, \tag{2.9}$$

and f^{abc} are the structure constants of the $SU(3)$ algebra.

2.1.1 CKM matrix

In the Standard Model of particle physics, the Cabibbo–Kobayashi–Maskawa (CKM) quark mixing matrix is the 3×3 unitary matrix that parameterizes the strength of the interactions of quarks with $W^\pm$ bosons, containing information on the rates of flavour-changing weak decays. This matrix was introduced for three generations of quarks by Makoto Kobayashi and Toshihide Maskawa, adding one generation to the matrix previously introduced by Nicola Cabibbo. Kobayashi and Maskawa were awarded one half of the 2008 Nobel Prize in Physics "for the discovery of the origin of the broken symmetry which predicts the existence of at least three families of quarks in nature" [7].

The charged-current $W^\pm$ interactions couple to the quarks with couplings given by:

$$
\begin{bmatrix}
V_{ud} & V_{us} & V_{ub} \\
V_{cd} & V_{cs} & V_{cb} \\
V_{td} & V_{ts} & V_{tb}
\end{bmatrix},
\tag{2.10}
$$

where in first order the probability for a quark of flavor i to decay into a quark of flavor j in the vertex $q_i \rightarrow q_j W^\pm$ is proportional to $|V_{ij}|^2$.

The CKM matrix elements are fundamental parameters of the SM, so their precise determination is important. Assuming unitarity and three families of quarks, the amplitudes were determined to be [4]:

$$
|V_{CKM}| =
\begin{bmatrix}
0.97419 \pm 0.00022 & 0.2257 \pm 0.0010 & 0.00359 \pm 0.00016 \\
0.2256 \pm 0.0010 & 0.97334 \pm 0.00023 & 0.0415^{+0.0010}_{-0.0011} \\
0.00874^{+0.00026}_{-0.00037} & 0.0407 \pm 0.0010 & 0.999133^{+0.000044}_{-0.000043}
\end{bmatrix}.
\tag{2.11}
$$

The CKM matrix tells us that the diagonal elements are dominant, meaning that the decays between each family are the most probable ones. For example, the top quark decays mainly to a W boson and a bottom quark.

These matrix elements can be parameterized in terms of three mixing angles (θ_{12}, θ_{23}, θ_{13}) between the generations and a *CP*-violating phase (δ). With the cosines and sines of

the angles denoted as c_{ij} and s_{ij}, respectively, a standard choice has become [4]:

$$V_{CKM} = \begin{bmatrix} c_{12}c_{13} & s_{12}c_{13} & s_{13}e^{-i\delta} \\ -s_{12}c_{23} - c_{12}s_{23}s_{13}e^{i\delta} & c_{12}c_{23} - s_{12}s_{23}s_{13}e^{i\delta} & s_{23}c_{13} \\ s_{12}s_{23} - c_{12}c_{23}s_{13}e^{i\delta} & -c_{12}s_{23} - s_{12}c_{23}s_{13}e^{i\delta} & c_{23}c_{13} \end{bmatrix}. \qquad (2.12)$$

At present, the best determined values for the sines of the angles are $\sin\theta_{12} = 0.2266^{+0.0025}_{-0.0023}$, $\sin\theta_{13} = 0.00387^{+0.35}_{-0.30}$ and $\sin\theta_{23} = 0.04113^{+1.37}_{-0.58}$ at a 68% confidence level [8].

It is important to note that the direct determination of $|V_{tb}|$ without assuming unitarity is possible from the single top quark production cross section. This will allow us to determine if the SM adequately describes the fundamental particles or if a fourth family is required.

2.2   Top Quark

The top quark is by far the heaviest of the known fundamental fermions in the SM of particle physics. In 1977 the discovery of the bottom quark indicated the existence of a third quark generation, and shortly after the search for the top quark began. Searches were conducted in electron-positron (e^+e^-) and proton-antiproton ($p\bar{p}$) collisions during the 1980s and early 1990s. Finally, in 1995, the top quark was discovered at the Fermilab Tevatron $p\bar{p}$ collider, by the CDF and D0 experiments [9, 10], at $\sqrt{s} = 1.8$ TeV.

The top quark mass was measured to be 173.1±1.3GeV/c^2 [11] and its electric charge is $+2/3|e|$. In Figure 2.1 the top quark mass measurements of the Tevatron experiments are summarized. It has been argued that the top quark could be the key to understand the dynamical origin of how particle masses are generated by the mechanism of electroweak symmetry breaking, since its mass is close to the energy scale at which the breakdown occurs (the vacuum expectation value of the Higgs field is ~246 GeV [12]).

Production and decay of top quarks provide a probe of the underlying dynamics, with minimal impact from the binding effects of QCD. Like any other quark in the SM, the top quark can decay only through the weak force, and dominantly to a W boson and a bottom quark, as shown in the previous section. However, its mean lifetime is 10^{-25}s, while the mean hadronization time is 10^{-24}s [13]. Since the top quark decays about an order of magnitude faster than the time needed to form bound states with other quarks, the spin information carried by the top quark is expected to be passed directly to their decay products. Therefore, because it decays before hadronizing and because of its mass being
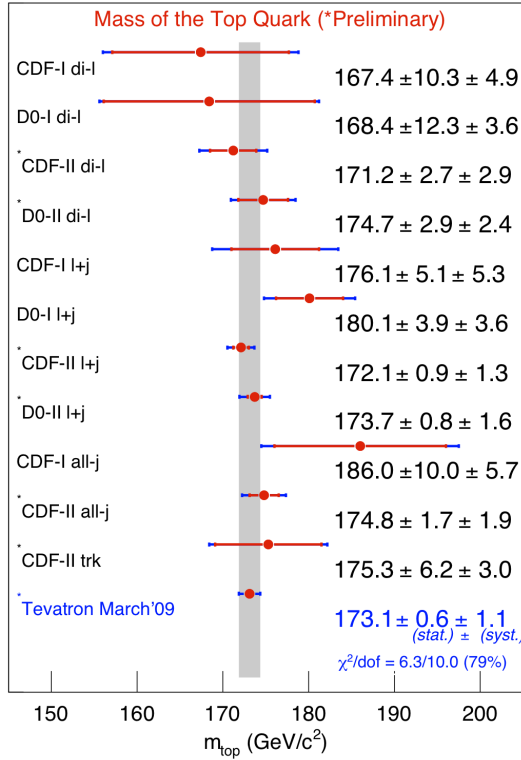
Figure 2.1: *Combined CDF and D0 mass measurements and resulting world average mass of the top quark. [11]*

close to the electroweak symmetry breaking scale, the top quark is an ideal probe for new physics beyond the SM and its properties can be studied with unprecedented accuracy.

In hadron colliders like the LHC, the top quark is mainly produced in pairs ($t\bar{t}$) via the strong interaction, by the processes $q\bar{q} \to t\bar{t}$ and $gg \to t\bar{t}$ (Figure 2.2). Unlike the Tevatron, the total production cross-section of $t\bar{t}$ in the LHC will be dominated by the gluon fusion process (90%). According to the SM, the top quark can also be produced by single production (single top) via the weak interaction, but with a lower cross section. This process will be the main subject of the next section.

The $t\bar{t}$ production cross section has been theoreticaly calculated at next-to-leading order (NLO), including next-to-leading logarithmic contributions (NLL) [14] and evaluated, approximately, at next-to-NLO (NNLO) with next-to-NLL (NNLL) contributions [15]. Assuming the Standard Model at NLO, the total cross section for the $t\bar{t}$ process is 833^{+52}_{-39} pb at 14 TeV [16]. The given errors include the uncertainties on the parton density functions (PDF), on the top quark mass and those due to the variation of the factorization and renor-

(a)

(b)
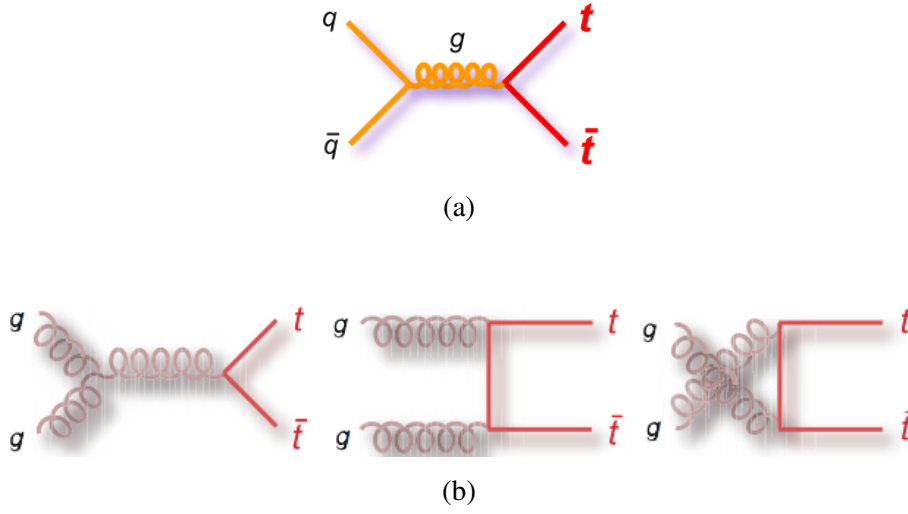
Figure 2.2: *Leading order Feynman diagrams for the $t\bar{t}$ process at the LHC: (a) quark anti-quark annihilation and (b) gluon fusion.*

malization scales, μ_F and μ_R. The first experimental observation of the $t\bar{t}$ process occurred in 1995 at the CDF and D0 experiments, measuring a cross section of $6.8^{+3.6}_{-2.4}$ pb [9] and 6.4 ± 2.2 pb [10], respectively, at $\sqrt{s} = 1.8$ TeV.

With a mass above the Wb threshold and V_{tb} close to unity, the decay width of the top quark is expected to be dominated by the two-body channel $t \to Wb$. The processes $t \to Ws$ and $t \to Wd$ are less probable because the corresponding CKM matrix elements are much smaller. Assuming three quark generations, the branching ratios are predicted to be $B(t \to Wb) = 99.8\%$, $B(t \to Ws) \simeq 0.19\%$ and $B(t \to Wd) \simeq 0.01\%$ [13]. The branching ratio of the $t \to Wb$ process is proportional to $|V_{tb}|^2$ in first order and its width is given, at Leading Order (LO), by:

$$\Gamma_{LO}(t \to Wb) = \frac{G_F}{8\pi\sqrt{2}} |V_{tb}|^2 m_t^3 \left(1 - 3\frac{M_W^4}{m_t^4} + 2\frac{M_W^6}{m_t^6} \right), \qquad (2.13)$$

where G_F is the Fermi constant, and m_t and m_W are the top quark and the W boson masses, respectively. Using the values $m_t = 171$ GeV and $m_W = 80.40$ GeV, the top quark width is $\Gamma = 1.44$ GeV/c^2 [13].

2.3   Single top quark production

The single top quark can be produced in three different channels: the t-channel (Figure 2.3a), the s-channel (Figure 2.3b) and the associated production or Wt-channel (Figure

2.3c). The definitions for these three channels are only valid at leading order, as higher order diagrams introduce mixing between the different production channels.

The single top production is less probable than the $t\bar{t}$ process. The NLO expected cross sections at 14 TeV are 66±2 pb for the Wt-channel [17], $246^{+11.8}_{-12.2}$ pb for the t-channel and $10.65^{+1.12}_{-1.02}$ pb for the s-channel [18]. The 7 TeV cross sections also calculated at NLO are: 13.102 pb for the Wt-channel, 58.723 pb and 3.937 pb for the t and s channels, respectively [19]. Since the LHC is a proton-proton collider, and there are twice as many valence up quarks as valence down quarks in the proton, the s and t channel cross sections for top production are larger than those for anti-top quark production by roughly a factor two. On the other hand, the top and anti-top quark cross sections are the same in the associated production channel, since no proton valence quarks are involved in this process (see Figure 2.3).

The experimental observation of the single top t and s channels was reported in 2009, by the Tevatron experiments [20, 21]. A combined cross section of $\sigma_{s+t} = 2.76^{+0.58}_{-0.47}$pb was obtained with $p\bar{p}$ collisions at a center of mass energy of 1.96 TeV, for a top quark mass of 170 GeV, with a total integrated luminosity of 3.2 fb^{-1} at CDF and 2.3 fb^{-1} at D0 [22]. In the same report, the CKM matrix element $|V_{tb}|$ was extracted with the value 0.88±0.07.

The Wt-channel is irrelevant at the Tevatron due to gluon luminosity and kinematics: this channel is produced from gluon-quark interaction, while at the centre of mass energy of $\sqrt{s} = 1.96$ TeV it is the quark-antiquark annihilation that dominates.

2.3.1 Single top Wt-channel

In the present thesis, the Wt-channel is studied, where an interaction between a gluon and a bottom quark coming from a gluon splitting in the proton sea results in the creation of a real W boson and a top quark.

The top quark decays mostly to a real W boson and a bottom quark. The W boson can decay leptonically or hadronically and a set of final state topologies are possible. Additionally, with the W boson from the associated production present, the single top Wt-channel can be divided into three different final state topologies:

1. Hadronic: both W bosons decay to a pair of quarks with a branching ratio of $67.60 \pm 0.27\%$ each [4]. The final topology is $bg \rightarrow Wt \rightarrow WWb \rightarrow q\bar{q}'q''\bar{q}'''b$.

2. Dileptonic: each one of the W bosons decays to an electron, a muon or a tau and the respective neutrino with a branching ratio of $32.40 \pm 0.16\%$[4]. The final topology is $bg \rightarrow Wt \rightarrow WWb \rightarrow l\nu_l l'\nu_{l'}b$, with $l = e, \mu, \tau$.

(a)

(b)

(c)
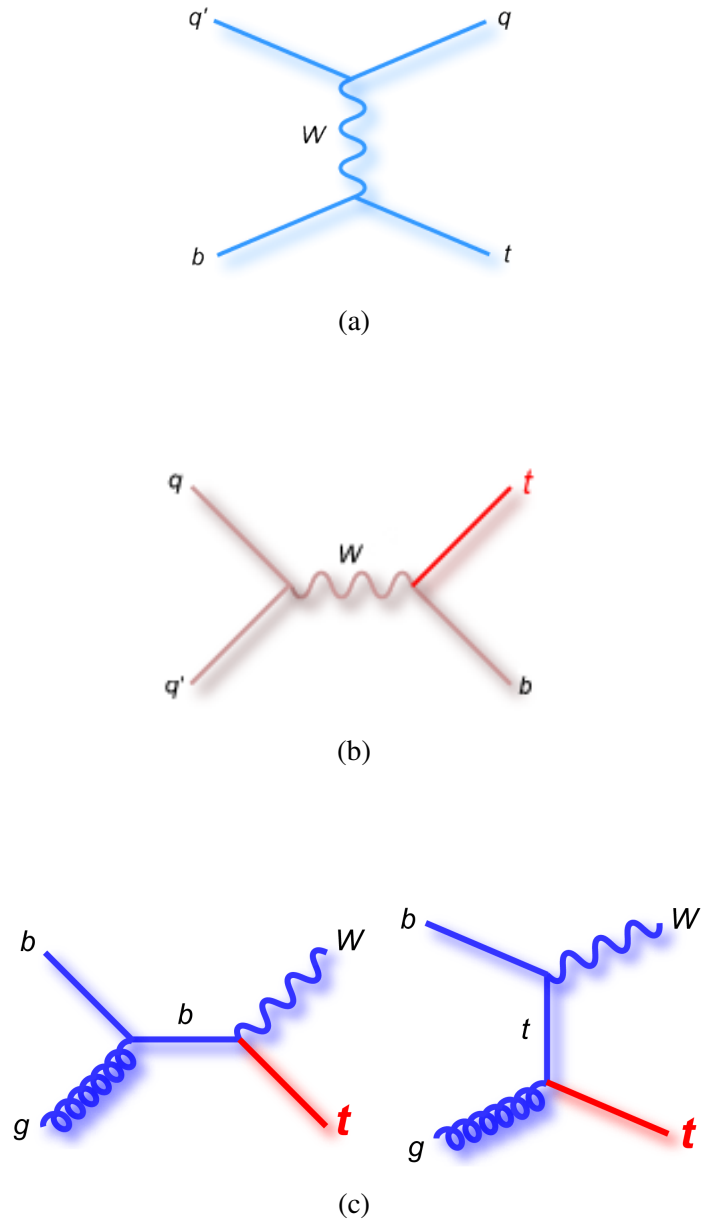
Figure 2.3: *Examples of leading order Feynman diagrams for the single top processes at the LHC: (a) t-channel; (b) s-channel and (c) Wt associated production.*
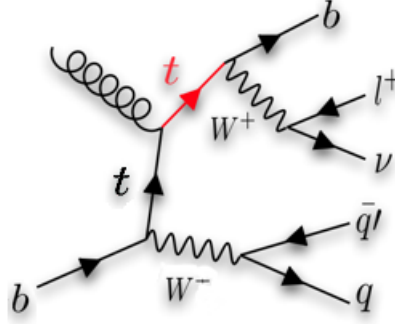
Figure 2.4: *Semileptonic single top Wt-channel. In this diagram, the W boson that decays hadronically is the one from the associated production.*

3. Semileptonic: one of the W bosons decays hadronically and the other leptonically, giving a final topology of $bg \to Wt \to WWb \to q\bar{q}'l\nu_l b$. In the present thesis, the W bosons of the Wt-channel will be referred to as leptonic or hadronic according to their decay channel.

The dileptonic topology has a clean signature due to the two high transverse momentum (p_T) leptons and the presence of missing energy. However, it has a smaller branching ratio and has disadvantages in the top quark reconstruction related to the two neutrinos escaping detection. On the other hand, the fully hadronic topology lacks a high p_T lepton, so the signal is not easily distinguishable from the abundant QCD multijets background. Therefore, in the present thesis the semileptonic topology is studied: the presence of a single high p_T lepton allows to suppress the SM W+jets and QCD background, while the p_T of the neutrino can be reconstructed as it is the only source of missing E_T for signal events.

A more detailed Feynman diagram describing the semileptonic single top Wt-channel is shown in Figure 2.4, at lowest order. The final state topology is characterized by the presence of two non b-tagged jets initiated by q and $\bar{q}'$, one lepton with high p_T, a single high-p_T b-tagged jet, and missing energy from the neutrino.

Considering now QCD NLO corrections to the Wt production, one finds that they include diagrams involving the production of an extra bottom quark, for example, the process $gg \to tW^-\bar{b}$ (and similar for the charge conjugate process). Such diagrams can also be thought of as the production of a top quark pair, with decay of $\bar{t}$ (t). A problem then occurs if the invariant mass of the final state Wb system is close to the top quark mass, making the propagator for the intermediate top quark large. It follows that the set of Feynman graphs contributing to $gg \to tW^-\bar{b}$ can be divided into two subsets, denoted as doubly resonant and singly resonant. The interference between these two subsets of graphs can be physi-

cally interpreted as the interference between Wt and $t\bar{t}$ production. Integrating over the total available phase space, the contribution from the $t\bar{t}$ amplitude to the cross section is, at the LHC, about one order of magnitude larger than the lowest order Wt cross section [23].

As mentioned earlier, one advantage of the study of single top production is the measurement of V_{tb}. Since the $t\bar{t}$ cross section is independent of the Wtb interaction, to investigate the Wt contribution alone these $t\bar{t}$ terms must be suppressed. Methods such as performing a cut on the invariant mass of the Wb system to prevent the t propagator from becoming resonant, or applying a veto to accept only low p_T additional b jets (typically 50 GeV) are proposed and studied in the literature. The particular method used for the generation of the events in this analysis is mentioned in section 4.1.

2.3.2 Anomalous couplings

The Wtb vertex lagrangian for on-mass-shell W, t and b, containing terms up to dimension five [24], can be written as:

$$\mathcal{L} = -\frac{g}{\sqrt{2}}\bar{b}\gamma^{\mu}\left(V_L P_L + V_R P_R\right)t W_{\mu}^{-} - \frac{g}{\sqrt{2}}\bar{b}\frac{i\sigma^{\mu\nu}q_{\nu}}{M_W}\left(g_L P_L + g_R P_R\right)t W_{\mu}^{-} + h.c., \quad (2.14)$$

where $q = p_t - p_b$ is the W boson momentum, $P_L = (1 - \gamma_5)$ and $P_R = (1 + \gamma_5)$ are the left and right-handed helicity projectors and $V_{L,R}\,(g_{L,R})$ are vector-like (tensor-like) couplings. If CP is conserved in the decay, the couplings can be taken as real numbers.

In the Standard Model, the Wtb vertex is purely left-handed, and its size is given by $V_L = V_{tb} \approx 1$, which can be measured in single top production. The anomalous couplings V_R, g_R and g_L vanish at the tree level but have small nonzero values at one loop level [25]. In new physics models, departures from the SM expectation $V_{tb} \simeq 1$ are possible.

These couplings can be related with the W boson helicity fractions in top quark decays. Therefore, the presence of anomalous couplings can change angular distributions and event kinematics, making the measurement of these observables important in the search for new physics. For example, studies of decay angular distributions provide a direct check of the V-A nature of the Wtb coupling and information on the relative coupling of longitudinal and transverse W bosons to the top quark.

Spin asymmetries are also a sensitive probe to new physics in the top quark production.

2.3.3 W boson polarization and angular asymmetries

The polarization of the W bosons emitted in the top quark decay is sensitive to the anomalous couplings. The spin-one real W boson in the $t \to Wb$ decay can be produced in three
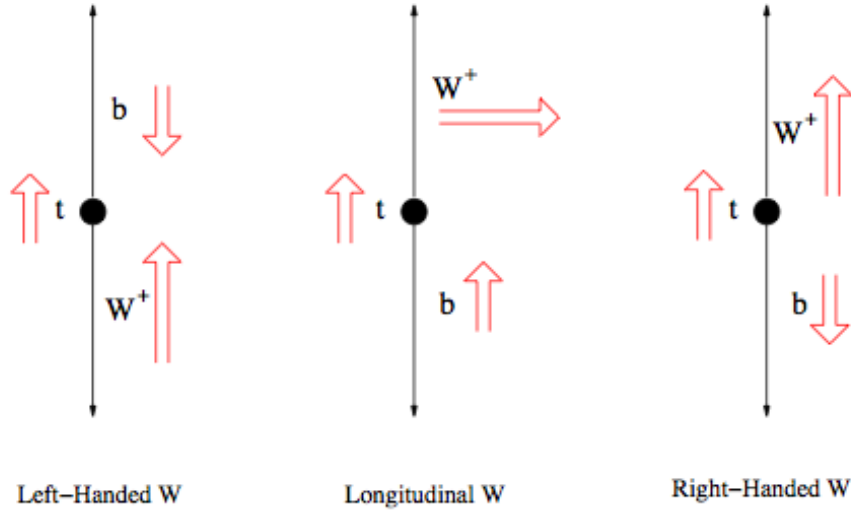
Figure 2.5: *Schematic representation of angular momentum conservation in $t \to W^+ b$ decay in the top quark rest frame. Simple arrows denote particle direction of motion and open arrows denote spin.*

different helicity states: positive (right-handed), negative (left-handed) or zero (longitudinal) helicity, as shown in Figure 2.5 for W^+ (opposite convention for W^-). The partial widths corresponding to the three states are Γ_R, Γ_L and Γ_0, with the total width being $\Gamma \equiv \Gamma(t \to Wb) = \Gamma_R + \Gamma_L + \Gamma_0$.

The corresponding helicity fractions are $F_0 = \Gamma_0/\Gamma$, $F_L = \Gamma_L/\Gamma$ and $F_R = \Gamma_R/\Gamma$, whose SM expectations, at leading order, tell us that the top quark decays to a longitudinally polarized W boson with a probability of 70.3%, while the left and right-handed W boson helicity states fractions are 29.7% and 0.036%, respectively, for $m_t = 175$ GeV, $m_b = 4.8$ GeV and $M_W = 80.39$ GeV [24]. Assuming a massless b-quark, the rightmost plot in Figure 2.5 is forbidden in the SM at tree level, since the b-quark must be left-handed. Therefore, right-handed W^+ bosons do not exist at tree level in the zero b-mass approximation, due to angular momentum conservation, and neither do left-handed W^-.

Information about the polarization states of the W boson is obtained from the angular distributions of one of its decay products. For example, the angle between the charged lepton momentum in the W rest frame and the W momentum in the t-quark rest frame (θ_ℓ^*) allows to study the W boson polarization. Alternatively, one may consider the angle $\theta_{\ell b}$ between the charged lepton and b-quark momenta in the W boson rest frame. Both approaches are equivalent since these two angles are related by $\theta_\ell^* + \theta_{\ell b} = \pi$. However, the experimental determination of $\theta_{\ell b}$ is simpler because both momenta are measured in the
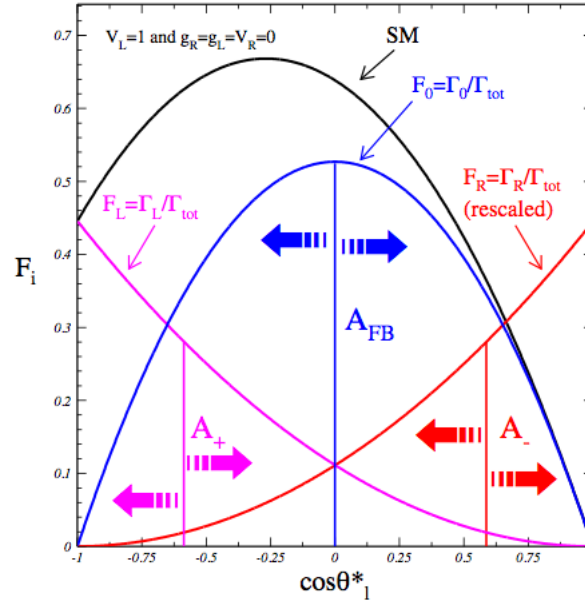
Figure 2.6: *Representation of angular distributions and asymmetries on the Wtb vertex for the SM and for its different components. The right-handed component F_R (red) is rescaled by a factor of 825.*

same reference frame.

The normalized differential decay rate for unpolarized top quarks can be written as [24]:

$$\frac{1}{\Gamma}\frac{d\Gamma}{d\cos\theta_\ell^*} = \frac{3}{4}\sin^2\theta_\ell^* F_0 + \frac{3}{8}(1-\cos\theta_\ell^*)^2 F_L + \frac{3}{8}(1+\cos\theta_\ell^*)^2 F_R, \qquad (2.15)$$

where interference terms due to different polarization states of the W boson do not contribute.

The Standard Model angular distribution is shown in Figure 2.6 in black, where it can be seen that it depends almost exclusively on the longitudinal and left-handed helicity fractions.

In the presence of anomalous couplings, the helicity fractions F_i are modified with respect to their SM values. Their dependence on the Wtb anomalous couplings was calculated in [24]:

$$F_0 = \frac{1}{\Gamma} \frac{g^2 |\vec{q}|}{32\pi} \{ \frac{m_t^2}{M_W^2} \left[V_L^2 + V_R^2 \right] \left(1 - x_W^2 - 2x_b^2 - x_W^2 x_b^2 + x_b^4 \right) + \left[g_L^2 + g_R^2 \right] \left(1 - x_W^2 + x_b^2 \right)$$

$$- 4x_b \left[V_L V_R + g_L g_R \right] - 2 \frac{m_t}{M_W} V_L [g_R - x_b g_L] \left(1 - x_b^2 \right) - 2 \frac{m_t}{M_W} V_R [g_L - x_b g_R] \left(1 - x_b^2 \right)$$

$$+ 2x_W V_L [g_R + x_b g_L] + 2x_W V_R [g_L + x_b g_R] \},$$

$$(2.16)$$

$$F_{R,L} = \frac{1}{\Gamma} \frac{g^2 |\vec{q}|}{32\pi} \{ \left[V_L^2 + V_R^2 \right] \left(1 - x_W^2 + x_b^2 \right) - 4x_b \left[V_L V_R + g_L g_R \right]$$

$$+ \frac{m_t^2}{M_W^2} \left[g_L^2 + g_R^2 \right] \left(1 - x_W^2 - 2x_b^2 - x_W^2 x_b^2 + x_b^4 \right) - 2 \frac{m_t}{M_W} V_L [g_R - x_b g_L] \left(1 - x_b^2 \right)$$

$$- 2 \frac{m_t}{M_W} V_R [g_L - x_b g_R] \left(1 - x_b^2 \right) + 2x_W V_L [g_R + x_b g_L] + 2x_W V_R [g_L + x_b g_R] \}$$

$$\pm \frac{g^2}{64\pi} \frac{m_t^3}{M_W^2} \{ -x_W^2 \left[V_L^2 - V_R^2 \right] + \left[g_L^2 - g_R^2 \right] \left(1 - x_b^2 \right) + 2x_W V_L [g_R + x_b g_L]$$

$$- 2x_W V_R [g_L + x_b g_R] \} \left(1 - 2x_W^2 - 2x_b^2 - 2x_b^2 x_W^2 + x_W^4 + x_b^4 \right).$$

$$(2.17)$$

The definitions $x_W = M_W/m_t$, $x_b = m_b/m_t$ and

$$|\vec{q}| = \frac{1}{2m_t} \left(m_t^4 + M_W^4 + m_b^4 - 2m_t^2 M_W^2 - 2m_t^2 m_b^2 - 2M_W^2 m_b^2 \right)^{1/2} \qquad (2.18)$$

for the norm of the W boson three-momentum in the top quark rest frame were used.

The variation of F_i with the anomalous couplings is plotted in Figure 2.7, considering that only one coupling is different from zero at a time and with the restriction to the CP-conserving case of real V_R, g_R and g_L. We observe that F_L and F_0 are much more sensitive to g_R than to g_L and V_R. On the other hand, F_R depends on the g_L and V_R couplings, but not on g_R.

A simple method to extract information about the Wtb vertex and determine the W boson helicity fractions is through angular asymmetries involving the angle θ_ℓ^*, defined as:

$$A_z = \frac{N(\cos \theta_\ell^* > z) - N(\cos \theta_\ell^* < z)}{N(\cos \theta_\ell^* > z) + N(\cos \theta_\ell^* < z)}, \qquad (2.19)$$

for any fixed value of z in the interval $[-1, 1]$, where N is the number of events.
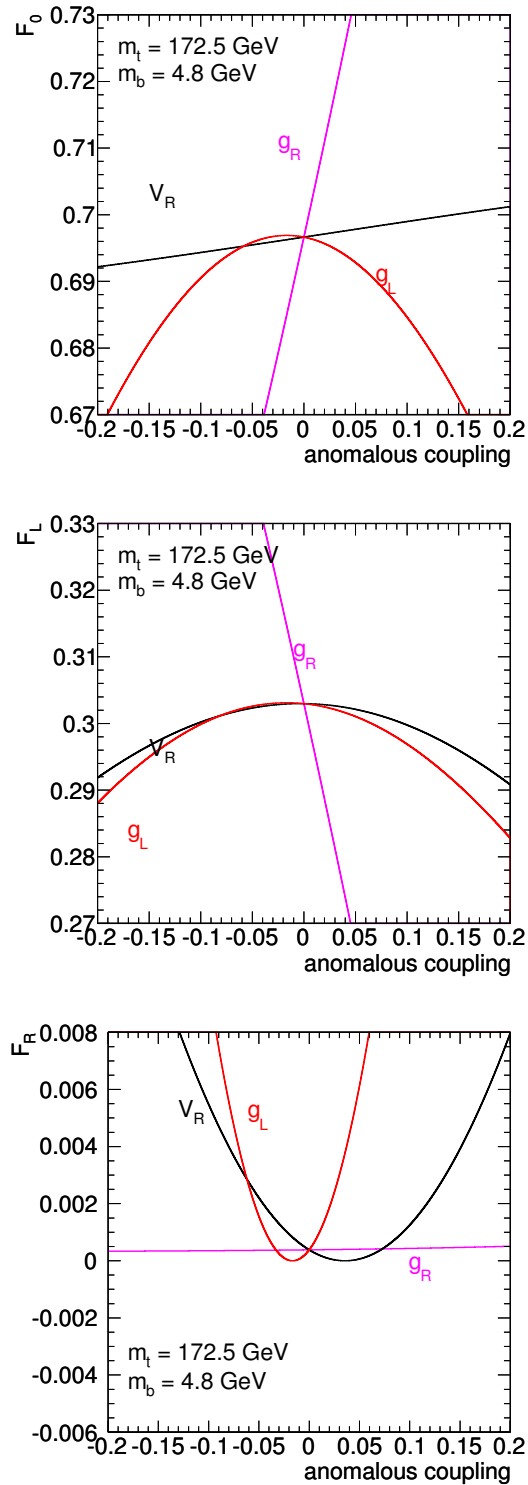
Figure 2.7: *Dependence on the anomalous couplings V_R, g_L and g_R of the helicity fractions (a) F_0, (b) F_L and (c) F_R.*

The forward-backward asymmetry, A_{FB}, is calculated with $z = 0$. This asymmetry is related to the W boson helicity fractions. With the SM distribution at leading order, the value for this observable is:

$$z = 0 \rightarrow A_{FB} = \frac{3}{4}(F_R - F_L) = -0.2225 \qquad (2.20)$$

To fully determine the $\cos\theta_\ell^*$ distribution, other asymmetries for different values of z must be considered. A_+ and A_- are chosen with $z = \mp(2^{2/3} - 1) = \mp\beta$ and so that they are not sensitive to the left and right-handed helicities, respectively. Again, at leading order:

$$z = -(2^{2/3} - 1) \rightarrow A_+ = 3\beta\left[F_0 + (1 + \beta)F_R\right] = 0.5482 \qquad (2.21)$$

$$z = (2^{2/3} - 1) \rightarrow A_- = -3\beta\left[F_0 + (1 + \beta)F_L\right] = -0.8397 \qquad (2.22)$$

The dependence of the three asymmetries A_{FB}, A_+, A_- on the anomalous couplings is shown in Figure 2.8, where it can be seen they all increase with g_R.

2.3.4 Spin asymmetries and top quark polarization

Additional angular asymmetries can be built from the top quark spin. Although the spins of the top quarks are not directly observable, they influence the angular distribution of their decay products. Top quarks are produced unpolarized at tree level in QCD interactions. However, according to the SM at leading order, the top quark is mostly left-handed in the single top quark production, with a polarization of approximately 0.89 [26].

For the dominant SM decay chain $t \rightarrow W^+ b \rightarrow \ell^+ \nu b, q\bar{q}'b$, the several decay products $i = \ell^+, \nu, q, \bar{q}', W^+, b$ can be used as "spin analysers". Their angular distribution in the top quark rest frame is given by [24]:

$$\frac{1}{\Gamma}\frac{d\Gamma}{d(\cos\theta_i)} = \frac{1}{2}\left(1 + P\alpha_i\cos\theta_i\right), \qquad (2.23)$$

where θ_i is the angle of the ith decay product momentum with the top quark spin direction and P is the top quark polarization. The constant α_i is called "spin analysing power" of the ith product and encodes the degree to which each decay product is correlated with the top quark spin [27]:
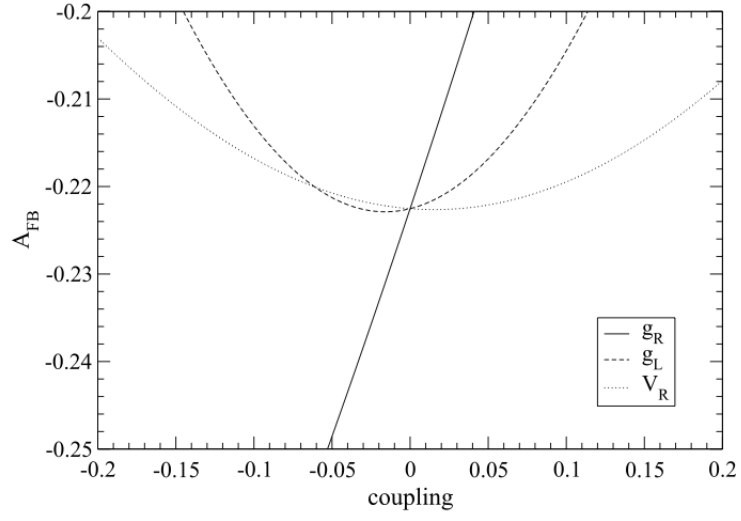
(a)
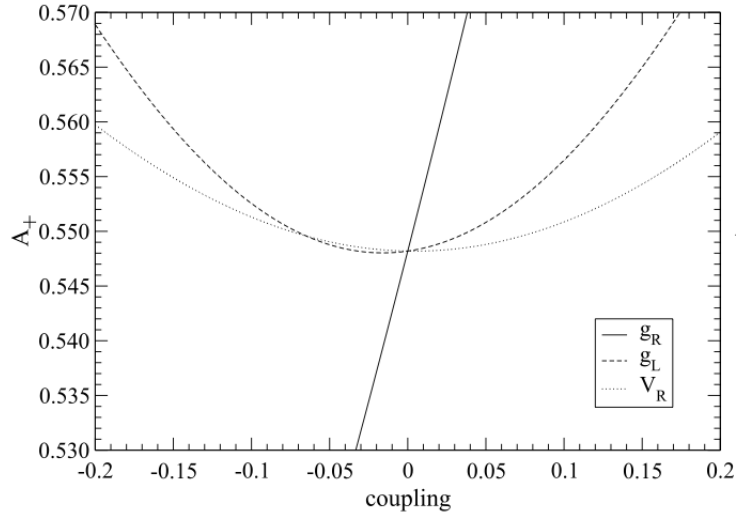
(b)
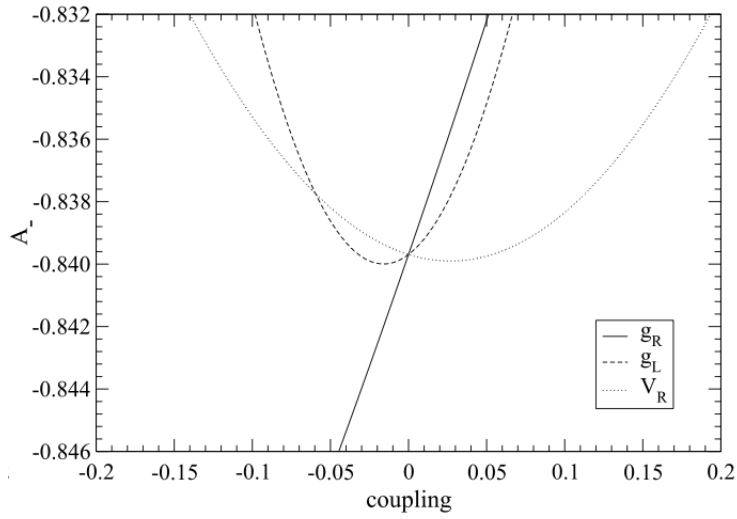
(c)

Figure 2.8: *Dependence on the anomalous couplings V_R, g_L and g_R of the angular asymmetries (a) A_{FB}, (b) A_+ and (c) A_-. [24]*

$$
\begin{cases}
\alpha_b = -\alpha_{W^+} = -0.40 \\[2em]
\alpha_\nu = \alpha_u = -0.33 \\[2em]
\alpha_{\ell^+} = \alpha_{\bar{d}} = 1.00
\end{cases}
.
$$

From these values for α_i we see that the charged lepton is maximally correlated with the top quark spin, which means that it is the best spin analyser. Therefore, the distribution of interest corresponds to the angle between the spin axis and the charged lepton in the top quark rest frame [28]. In Figure 2.9 the SM distributions at leading order of equation 2.23 are shown. Assuming that CP is conserved in the decay, the distributions are the same for the antiparticles, but with $\alpha_{\bar{i}} = -\alpha_i$.

Using equation 2.23 for each spin analyser, the spin asymmetries are defined as:

$$
A_i = \frac{N(\cos\theta_i > 0) - N(\cos\theta_i < 0)}{N(\cos\theta_i > 0) + N(\cos\theta_i < 0)} = \frac{1}{2}P\alpha_i.
\tag{2.24}
$$

Calculated at leading order in the Standard Model, these spin asymmetries take the following values [27]:

$$
\begin{cases}
A_\ell = 0.445 \\[2em]
A_\nu = -0.142 \\[2em]
A_b = -0.181
\end{cases}
.
$$

Spin asymmetries are more sensitive to anomalous couplings in the single top production than in the $t\bar{t}$ process. Therefore, single top quark production is an important tool to search for new physics at the Wtb vertex.
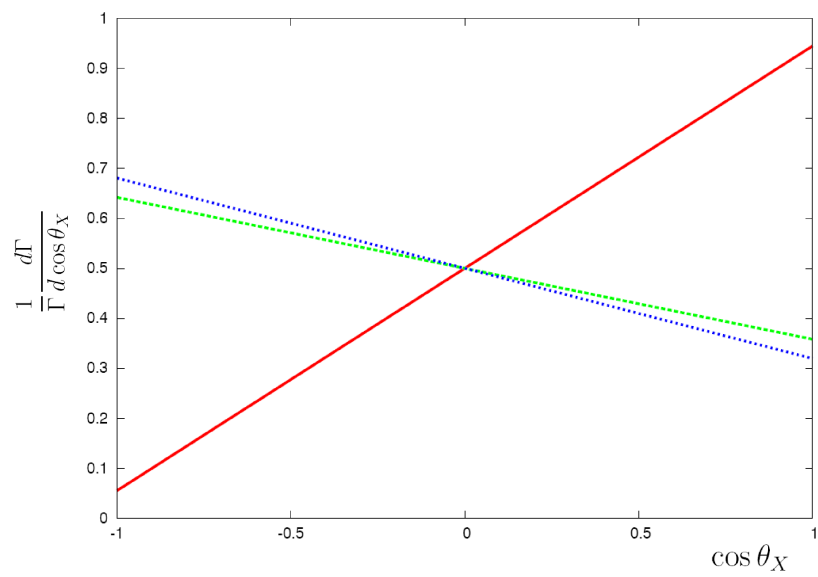
Figure 2.9: *Spin distributions in the decay of a top quark for the lepton (red), neutrino (green) and b-jet (blue). The lines are the distributions of the angle between the top quark spin axis and the particle three-momentum in the rest frame of the top quark. [27]*

Chapter 3

ATLAS Detector

This chapter introduces the CERN laboratory and the Large Hadron Collider (LHC). The ATLAS detector and its performance, as well as the trigger and data acquisition systems are shortly described.

3.1 CERN

One of the world's largest centres for scientific research is CERN - the European Organization for Nuclear Research. It is located on the french-swiss border near Geneva, Switzerland. CERN is currently run by 20 European Member States and used by many other European and non-European countries.

Since it was established in 1954, CERN has played a role on major scientific and technological achievements in particle physics and computer science, including the discovery of W and Z bosons (1983) and the development of the World Wide Web (1990). More recently, in 1995, the laboratory succeeded in creating anti-matter atoms and in 2000 there was the first evidence for the quark-gluon plasma state of matter. Finally, on the 30th of March of 2010 the laboratory succeeded in the first attempt to collide protons at 7 TeV of centre of mass energy.

3.2 LHC

The Large Hadron Collider is a proton-proton collider located at CERN. The LHC project was approved by the CERN Council in December 1994 and had its first collisions in November of 2009. With its unprecedented high energy and luminosity, the LHC will extend the frontiers of particle physics.

The 27 km circular tunnel is located at a depth of about 100 metres underground that was previously occupied by the Large Electron-Positron Collider (LEP), which accelerated electrons and positrons to a centre of mass energy up to $\sqrt{s} = 209$ GeV.

Proton beam energy at collision	7 TeV
Proton beam energy at injection	0.45 TeV
Number of particles per bunch	1.15×10^{11}
Number of bunches	2808
Circulating beam current	0.584 A
Stored Energy per beam at collision	362 MJ
Mean bunch length at collision	7.55 cm
Peak luminosity (ATLAS and CMS)	$1.0 \times 10^{34} cm^{-2} s^{-1}$
Inelastic cross section	60.0 mb
Total cross section	100.0 mb

Table 3.1: *LHC nominal beam parameters. [29]*

Currently, the LHC accelerates proton beams to a centre of mass energy of $\sqrt{s} = 7$ TeV and is expected to achieve in the future its design center of mass energy of 14 TeV with a nominal luminosity of 10^{34} cm^{-2}s^{-1}. Heavy ions, in particular lead nuclei, can also be accelerated but their study is beyond the scope of the present thesis.

During the stable beams at $\sqrt{s} = 7$ TeV, the total integrated luminosity in proton-proton collisions delivered by the LHC up until middle of July 2010 was about 161 nb^{-1}. This amounts to a total of ~ 148 nb^{-1} of integrated luminosity recorded by the ATLAS detector (see Figure 3.1). Currently, dedicated machine development is being made in order to increase the instantaneous luminosity delivered by the machine. The expected integrated luminosity delivered to the experiments in proton-proton collisions under nominal conditions is about $\mathscr{L} = 100$ fb^{-1} per year, per experiment (ATLAS and CMS).

The protons will be organized in bunches of up to 10^{11} protons (p) and at full luminosity there will be approximately 20 proton-proton collisions per bunch crossing [29]. Some of the relevant LHC parameters are summarized in Table 3.1.

Since the protons will travel at a speed very close to the speed of light, high magnetic fields are necessary to bend their trajectory inside the vacuum tube. This can be achieved with low temperature superconducting magnets. The LHC tunnel has 1232 dipole magnets and 392 quadrupoles. The dipoles are used to keep the particles in nearly circular orbits while the quadrupoles focus the beams. The magnets are made of superconducting niobium-titanium (Ni-Ti) cables and are kept at 1.9 K using superfluid helium for cooling
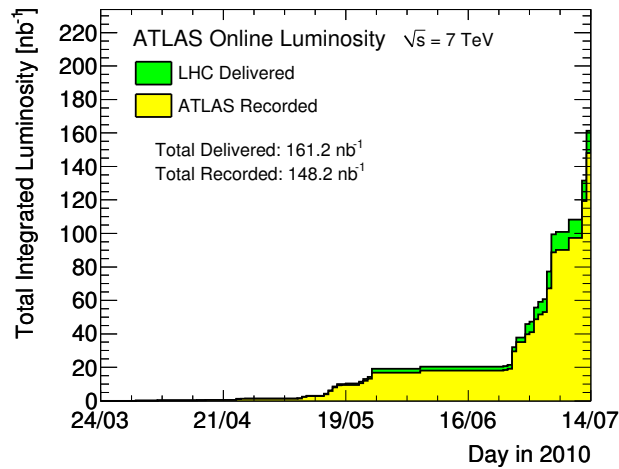
Figure 3.1: *Cumulative luminosity versus day, delivered to (green) and recorded by ATLAS (yellow) during stable beams and for 7 TeV centre-of-mass energy. The systematic uncertainty of the luminosity measurement is estimated to be 11%.*

and producing a magnetic field of 8.33 T. The beams are accelerated and kept at a constant energy through eight superconducting radio frequency (RF) cavities per beam, operating at 4.5 K [29].

The proton beams will collide at four interaction points that correspond to where the four major detectors are placed: ATLAS [30], CMS [31], ALICE [32] and LHCb [33] (Figure 3.2).

ATLAS and CMS are two general purpose detectors built for studying proton and ions collisions and dedicated, for example, to the Higgs boson and dark matter candidates research fields. ALICE is a dedicated heavy-ion detector that will study the physics of strongly interacting matter at extreme energy densities, where the formation of a new phase of matter, the quark-gluon plasma, is expected. LHCb will perform precise measurements of CP violation and rare decays on bottom quark physics. Two other smaller detectors meant for specialized research are TOTEM [34], an experiment to measure total cross sections, elastic scattering and diffraction dissociation at the LHC; and LHCf [35], for the measurement of photons and neutral pions in the very forward region of the LHC.
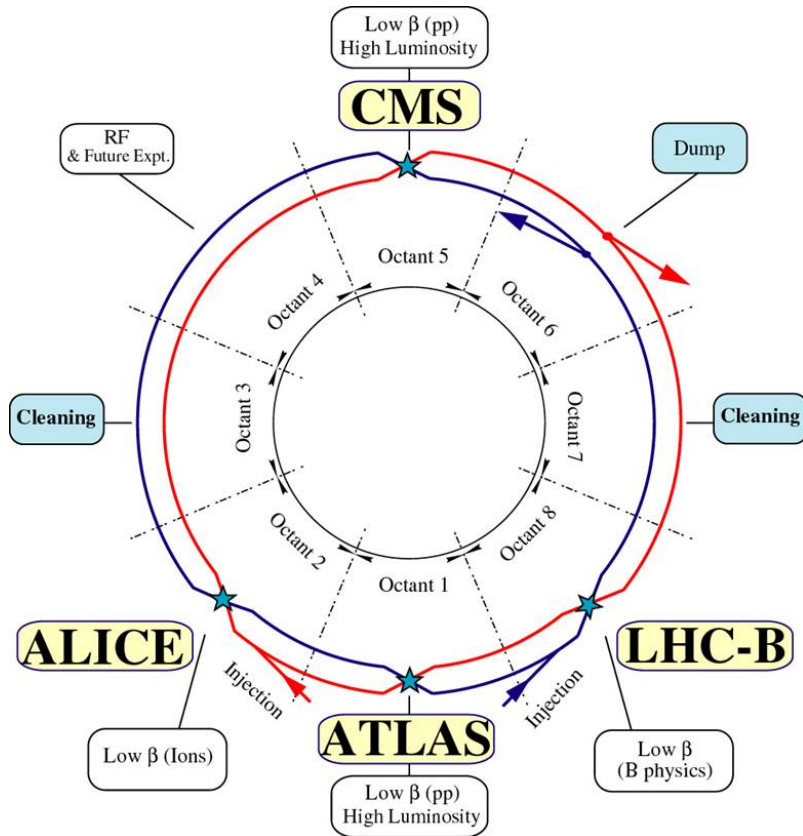
Figure 3.2: *Schematic representation of the LHC circular tube. The four main experiments are shown, as well as the two tubes where the beams circulate.*
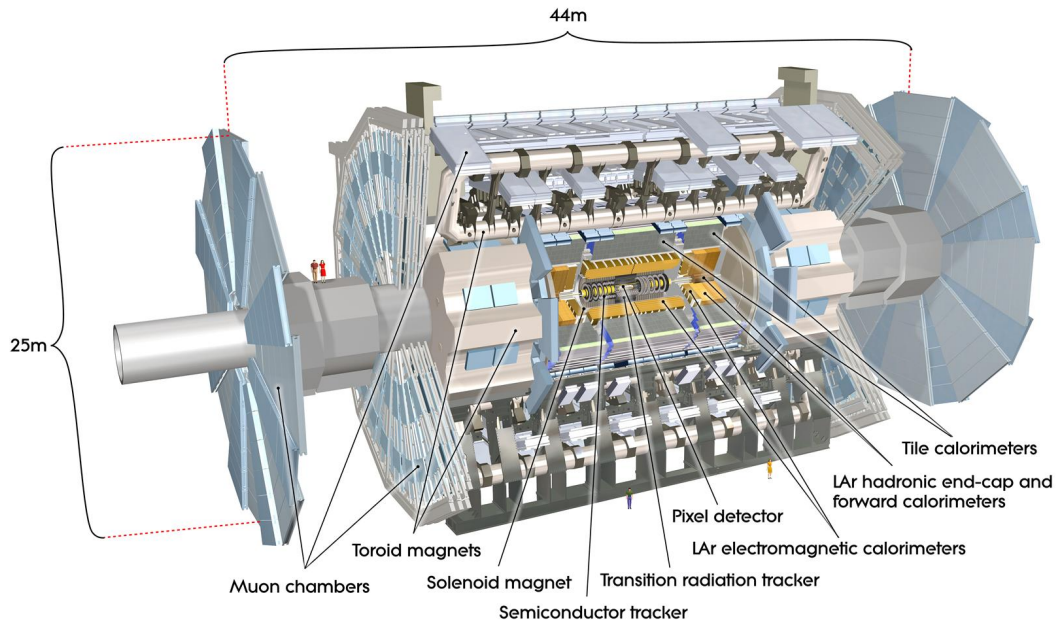
Figure 3.3: *Cut-away view of the ATLAS detector, its subdetectors and magnets.*

3.3 ATLAS

The ATLAS Detector, the name standing for **A T**oroidal **L**HC **A**pparatu**S**, is situated at the Octant 1 of the LHC (see Figure 3.2).

Common to many high energy physics detectors, ATLAS has a set of dedicated subdetectors in a cylindrical barrel plus end-caps structure, in order to cover the maximum possible solid angle around the interaction point. The detector is about 44 metres long, 25 metres in diameter and weighs approximately 7000 tonnes [36]. It is nominally forward-backward symmetric with respect to the interaction point. The overall ATLAS detector layout is shown in Figure 3.3.

The ATLAS detector consists of four major components: the Inner Detector which measures the momentum of each charged particle, the calorimeters which measure the energy carried by the particles, the muon spectrometer which identifies and measures muons, and the magnet system that bends charged particles for momentum measurement. Hence, in this experiment it will be possible to identify and measure the momentum, energy and electric charge of all stable particles produced (except for the neutrino). These four components are described with more detail further on.

The nominal interaction point is defined as the origin of the ATLAS coordinate system,
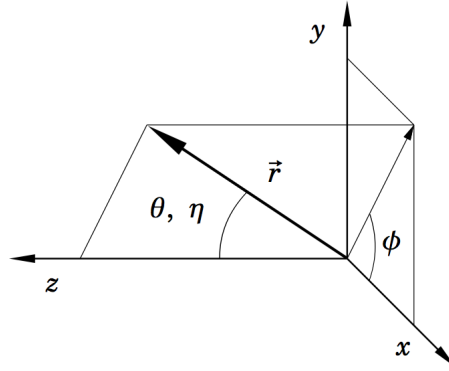
Figure 3.4: *ATLAS coordinate system.*

while the beam direction defines the z-axis (positive z pointing to the LHCb detector, see Figure 3.2) and the $x - y$ plane is transverse to the beam direction (see Figure 3.4). The positive x-axis is defined as pointing from the interaction point to the centre of the LHC ring and the positive y-axis is defined as pointing upwards. The azimuthal angle ϕ is measured as usual around the beam axis, and the polar angle θ is the angle measured from the beam axis.

An important variable in ATLAS is the pseudo-rapidity, defined as $\eta = -\ln \tan(\theta/2)$. The ATLAS detector has full ϕ coverage and a pseudo-rapidity coverage reaching $|\eta| = 2.5$ for tracking systems and $|\eta| \simeq 5.0$ for calorimetry. The momentum in the transverse plane is defined as $p_T = \sqrt{p_x^2 + p_y^2}$. The transverse energy E_T and the missing transverse energy E_T^{miss} are defined in the $x - y$ plane. The distance ΔR in the pseudo-rapidity - azimuthal angle space is defined as $\Delta R = \sqrt{\Delta \eta^2 + \Delta \phi^2}$.

The high interaction rates, radiation doses, particle multiplicities and energies, as well as the requirements for precision measurements have set the standards for the design of particle detectors. Viewed in this context, these benchmark physics goals were turned into a set of general requirements for the detector [36]:

- Fast, radiation-hard electronics and sensor elements; high detector granularity to reduce the influence of overlapping events.

- Large acceptance in pseudo-rapidity with almost full azimuthal angle coverage.

- Good charged-particle momentum resolution and reconstruction efficiency in the Inner Detector.

- Very good electromagnetic calorimetry for electron and photon identification and

Component	Required resolution	η coverage	
		Measurement	Trigger
Tracking	$\sigma_{p_T}/p_T = 0.05\% \cdot p_T \oplus 1\%$	±2.5	
EM calorimetry	$\sigma_E/E = 10\%/\sqrt{E} \oplus 0.7\%$	±3.2	±2.5
Hadronic calorimetry (jets)			
barrel and end-cap	$\sigma_E/E = 50\%/\sqrt{E} \oplus 3\%$	±3.2	±3.2
forward	$\sigma_E/E = 100\%/\sqrt{E} \oplus 10\%$	3.1<$|\eta|$<4.9	3.1<$|\eta|$<4.9
Muon spectrometer	$\sigma_{p_T}/p_T = 10\%$ at $p_T = 1$ TeV	±2.7	±2.4

Table 3.2: *General performance goals of the detector components. The unit for E and p_T is GeV.* [36]

measurements; full-coverage hadronic calorimetry for accurate jet and missing transverse energy measurements.

- Good muon identification and momentum resolution over a wide range of momenta; ability to determine unambiguously the charge of high p_T muons.

- Highly efficient triggering on low transverse-momentum objects with sufficient background rejection.

- Forward detectors, aimed to determine the luminosity delivered to ATLAS.

ATLAS detector main performance goals are listed in Table 3.2.

3.3.1 Magnet system

The purpose of the magnet system is to bend the trajectory of the charged particles produced, allowing to measure their momenta and charge sign.

The ATLAS magnet configuration [36] comprises a thin superconducting solenoid surrounding the inner-detector cavity, and three large superconducting toroids (one barrel and two end-caps) arranged with an eight-fold azimuthal symmetry around the calorimeters (Figure 3.5). This fundamental choice has driven the design of the rest of the detector.

The solenoid has an inner and outer diameter of 2.46 m and 2.56 m respectively and is 5.8 m long, creating a 2 T axially symmetric magnetic field for the inner detector. This field is nearly uniform and strong enough to bend very energetic particles.

The barrel and the two end-cap toroids produce a toroidal magnetic field for the muon detectors. The barrel toroid is 25.3 m long, has an inner and outer radius of 9.4 m and 20.1 m and covers the region $|\eta| < 1.0$, producing a 0.5 T magnetic field. The end-cap
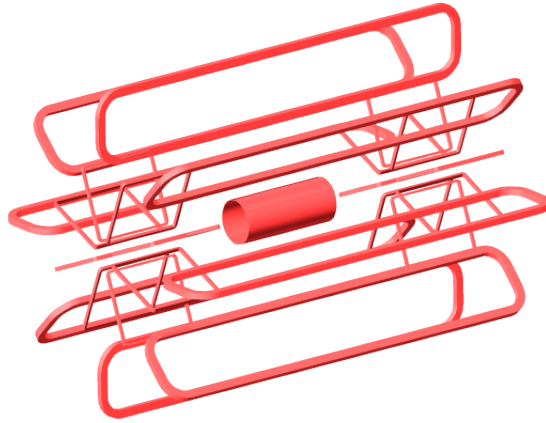
Figure 3.5: *Schematic representation of the magnet system: the solenoid, the barrel toroid and the end-cap toroids.*

toroids are 5.0 m long, have an inner diameter of 1.65 m and an outer diameter of 10.7 m, cover the region $1.4 < |\eta| < 2.7$ and produce a magnetic field of 1 T.

3.3.2   Inner Detector

The Inner Detector [36] is the ATLAS tracking system, dedicated to the reconstruction of the charged particles trajectories, the measurement of their momenta and their identification. The high number of tracks produced in each collision requires very good momentum resolution and granularity.

It is the layer closest to the beam pipe, extending to a radius of about 1 m. It is 6 m long and is divided in three parts and technologies: the Pixel Detector, the Semiconductor Tracker (SCT) and the Transition Radiation Tracker (TRT), all immersed in a 2 T solenoid field (Figure 3.6).

The Pixel Detector is the one closest to the interaction point and consists of 3 cylindrical layers of pixel sensors and microstrips. It must be very resistant to radiation, given its location.

The SCT is made of semiconductor strips and measures particles over a much larger area than the Pixel Detector, which means it is useful for tracking in the transverse plane.

In the barrel region, both the Pixel Detector and the SCT are arranged in concentric cylinders around the beam axis, covering the region $|\eta| < 2.5$. At the end-cap regions they are arranged in disks perpendicular to the beam axis.

Finally, the TRT detects the transition radiation produced by relativistic charged particles that cross the interface of materials with different electrical properties. Since the prob-
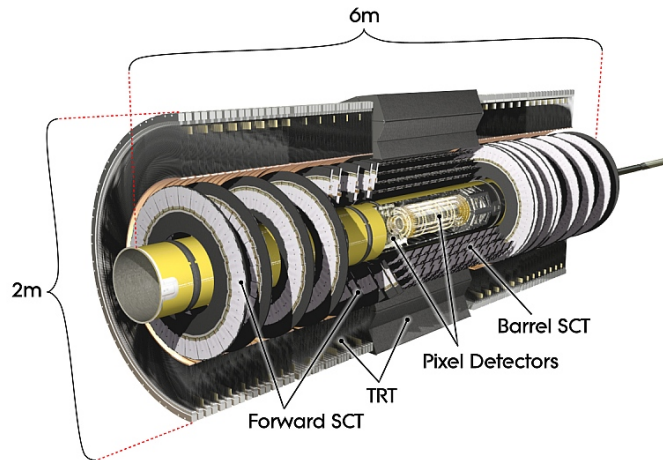
Figure 3.6: *Schematic representation of the Inner Detector.*

ability of the transition radiation increases with the relativistic gamma factor $\gamma = E/mc^2$, it is possible to discriminate between lighter and heavier particles. This detector consists of a large number of straw tubes with a xenon gas mixture.

3.3.3 Calorimeters

The calorimeter system of ATLAS is composed by the electromagnetic and the hadronic calorimeters (Figure 3.7). An electromagnetic calorimeter is designed to identify and measure the energy of the particles that interact primarily via the electromagnetic force. On the other hand, a hadronic calorimeter is designed to measure the energy of the particles that interact via the strong force. The calorimeters must provide good containment for the electromagnetic and hadronic showers that are initiated by the particles, limiting those that reach the muon detectors.

The electromagnetic calorimeter of ATLAS [36] is a sampling calorimeter made of layers of lead as the passive material and liquid argon (LAr) as the active material. It has an accordion geometry with full azimuthal symmetry, covering the region $|\eta| < 3.2$. The EM calorimeter is divided into three parts: the barrel ($|\eta| < 1.475$) and two end-caps ($1.375 < |\eta| < 3.2$).

The hadronic calorimeter [36] is composed of three subdetectors: the LAr hadronic end-cap calorimeter (HEC), the LAr forward calorimeter (FCal) and the tile calorimeter (TileCal). HEC is a copper/LAr sampling calorimeter covering the range $1.5 < |\eta| < 3.2$. It is located in the end-cap region and consists of two wheels with a 2.03 m radius. FCal
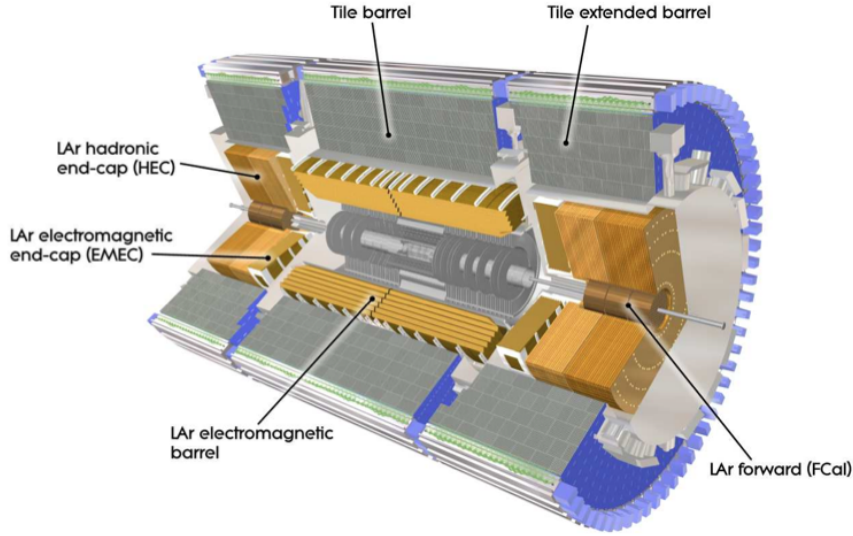
Figure 3.7: *Schematic representation of the calorimeters of ATLAS.*

is also composed by copper/LAr and is located in the forward region, at 4.5 m from the interaction point. It covers the region $3.1 < |\eta| < 4.9$, overlapping HEC. Its purpose is to minimize the loss of energy and to reduce background radiation levels in the forward muon spectrometer.

TileCal [37] is a sampling calorimeter of steel (passive material) and scintillator (active material). It is located behind the LAr EM calorimeter, covering the region $|\eta| < 1.7$ and extending from an inner radius of 2.28 m to an outer radius of 4.25 m. It is divided in one long central barrel ($|\eta| < 1.0$) and two extended barrels ($0.8 < |\eta| < 1.7$), each built of 64 independent wedges along the azimuthal direction. The light produced in the scintillating tiles is collected at the edges of each tile using two wavelength shifting fibers that are connected to photomultipliers.

The portuguese ATLAS group is strongly involved in the TileCal laser monitoring system of the photomultiplier tubes (PMTs), in the taking, reconstruction and analysis of Tile-Cal cosmic muon commissioning data and on the description of the noise behaviour of the TileCal (see for example Ref.[38]).

3.3.4   Muon Spectrometer

The calorimeter system is surrounded by the muon spectrometer, whose function is to efficiently identify muons and measure their momentum. It is the most external subdetector of ATLAS, extending from a radius of 4.25 m to the outer radius of the detector. The work
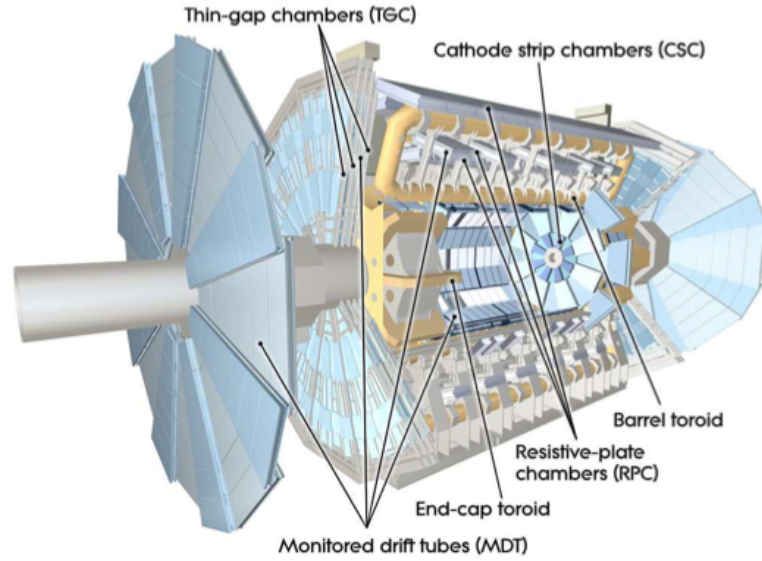
Figure 3.8: *Schematic representation of the muon system.*

principle of the Muon Spectrometer [36] is similar to the Inner Detector's, being based on the magnetic deflection of muon tracks to measure their momentum.

The magnetic field is provided by an air-core toroid system, with a long barrel covering the region $|\eta| < 1.4$ and two end-cap magnets inserted on both ends of the barrel covering the region $1.6 < |\eta| < 2.7$. The $1.4 < |\eta| < 1.6$ transition region has a combination of barrel and end-cap fields.

In the barrel region, tracks are measured in chambers arranged in three cylindrical layers around the beam axis, while in the end-cap regions the chambers are placed vertically, also in three layers.

The Muon Spectrometer is composed of four different tracking detector technologies (see Figure 3.8): Monitored Drift Tubes (MDT), which are aluminium-walled gaseous drift chambers where muons ionize the gas under a high electric field; Cathode Strip Chambers (CSC), precision detectors in the barrel and end-cap region, which are multiwire proportional chambers with cathodes segmented into strips; Resistive Plate Chambers (RPC) and Thin Gap Chambers (TGC) that compose the muon trigger system.

3.3.5 Trigger and data acquisition system

At the design luminosity of 10^{34} cm^{-2}s^{-1} the bunches of protons will cross each other at 40 MHz. Only a small fraction of these interactions, at approximately 1 GHz, results in

interesting physics processes. However, the event data recording, based on technology and resource limitations, has to select a manageable rate of such events for permanent storage and further analysis: about 200 Hz. This requires an overall rejection factor of $\sim 10^7$ against minimum-bias processes while maintaining maximum efficiency for new physics.

The trigger and data acquisition system (TDAQ) [39] has three distinct levels: L1, L2 and the Event Filter. The latter two (L2 and EF) are part of the High Level Trigger (HLT). The schematic representation of the three levels is shown in Figure 3.9. Each trigger level refines the decisions made at the previous level and, where necessary, applies additional selection criteria.

L1 uses a limited amount of the total detector information to make a decision in less than 2.5 μs, reducing the rate to about 75 kHz. Meanwhile, the full event data is kept in the pipeline memory. Its decision is based on the search for high-p_T muons, electrons, photons, jets, and τ-leptons decaying into hadrons, as well as large missing and total transverse energy. In each event, L1 trigger defines Regions-of-Interest (RoI's), i.e., the η-ϕ coordinates of those regions within the detector where its selection process has identified interesting features.

L2 selection uses all the available detector data within the RoI's, reducing the trigger rate to approximately 3.5 kHz. The final stage of the event selection, the Event Filter, which uses off-line procedures to fully reconstruct the events, reduces the event rate to roughly 200 Hz. Those events that fulfill this last selection criteria are finally stored in the permanent event storage.

The portuguese ATLAS team has also a collaboration in the Trigger and DAQ system for the ATLAS experiment.

3.3.6   GRID

The LHC will produce roughly 15 petabytes of data annually. Thousands of scientists around the world want to access and analyse this data, so CERN is collaborating with institutions in 34 different countries to operate a distributed computing and data storage infrastructure: the Worldwide LHC Computing Grid (LCG) [40].

Data from the LHC experiments is distributed around the globe, with a primary backup recorded on tape at CERN, the Tier-0. After initial processing, this data is distributed to eleven large computer centres with sufficient storage capacity for a large fraction of the data, and with round-the-clock support for the computing grid. These so-called Tier-1 centres make the data available to over 160 Tier-2 centres for specific analysis tasks. Individual scientists can then access the LHC data from their home country, using local computer clusters (Tier-3) or even individual PCs.
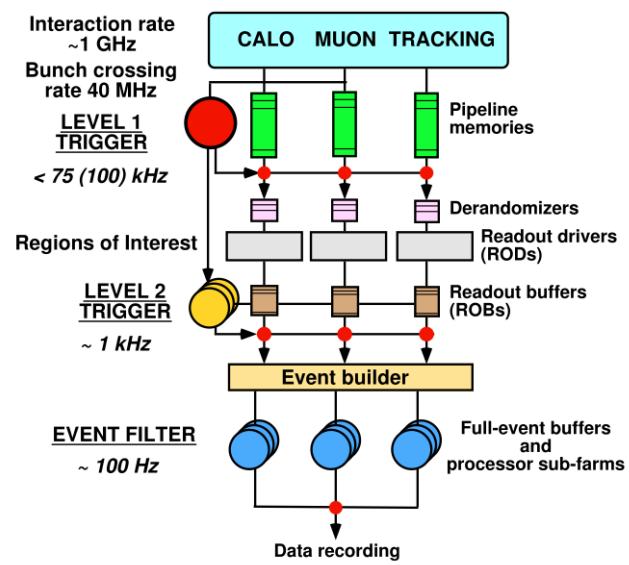
Figure 3.9: *Scheme of the ATLAS trigger and data acquisition system.*

Chapter 4

Generation and Simulation of Events

In this chapter, the Monte Carlo (MC) generators used for all the relevant processes are presented, as well as the libraries used for the simulation of events in the ATLAS detector. The subsequent identification and reconstruction of the physics objects in the final state is described.

4.1 Event Generation

To explore the physical properties of all the processes under study, large samples of simulated events are needed. Firstly, these events are generated with MC techniques. The generation of both the signal and the remaining SM processes is described in this section.

The generation of pp interactions in MC programs is possible through factorization, which allows to decouple the short distance perturbative hard interaction among the parton constituents from the long range physics related to the parton momentum distributions, the final-state hadron formation and further soft interactions, referred to as the underlying event. This separation introduces a factorization scale [41].

The high energy processes originating from pp collisions were generated using both leading order (LO) and next-to-leading order (NLO) Monte Carlo programs. The samples were generated with a centre of mass energy of 7 TeV and the top quark and W boson masses were assumed to be $m_t = 172.5$ GeV and $m_W = 80.40$ GeV, respectively.

The calculation of production cross sections at a hadron collider like LHC depends on the knowledge of the Parton Distribution Functions (PDF). The PDF's are probability distributions of the momentum fraction (x) of quarks and gluons inside a proton, defined as a function of the squared momentum transfer carried by the exchanged particle (Q^2). The
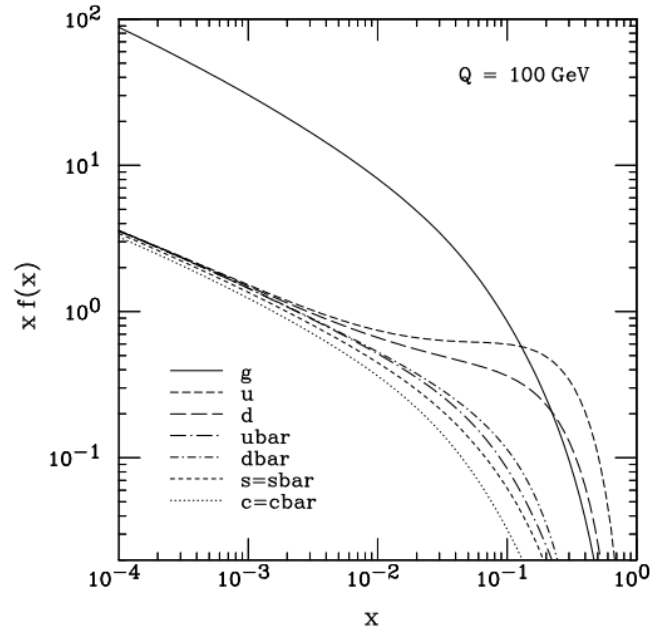
Figure 4.1: *Parton distribution functions for $Q = 100$ GeV by CTEQ6M.*

differential cross section for a general hadron-hadron collision is given by:

$$\frac{d\sigma}{d\Omega dx_1 dx_2} \propto \sum_{i,j,k,...,n} f_i(x_1, \mu_F) f_j(x_2, \mu_F) \times \bar{\sum} |M(i, j \to k, l, ..., n)|^2. \qquad (4.1)$$

The function f_i is a PDF corresponding to parton i with momentum fraction x_1 in a proton probed at a scale μ_F. The first summation is over all n partons within the proton, and the inner summation represents the average and sum over helicity and colors. $|M|^2$ represents the square of the matrix element for the process of interest.

The PDF's cannot be calculated perturbatively because of the inherent non-perturbative nature of a QCD binding state. Therefore, the known PDFs are obtained from experimental data. In Figure 4.1 a distribution evaluated by the CTEQ Collaboration [42] is shown for a scale of $Q = 100$ GeV. For the calculation of the leading order cross sections the CTEQ6L set of structure function parametrizations was used, while processes available at NLO were calculated using the CTEQ6M parametrizations.

The color confinement of quarks and gluons implies that they cannot be directly observed, forming instead jets of color-neutral hadrons that will be detected. Such process is called hadronization and is simulated by Monte Carlo methods such as HERWIG [43] and PYTHIA [44].

Single top events for the three channels were generated with MC@NLO 3.4 Next-to-

Process	Generator	σ (pb)	N_{events}	$\mathscr{L}$ (fb^{-1})
Wt-channel	MC@NLO	14.581	14995	1.028
t-channel	MC@NLO	21.456	29990	1.398
s-channel	MC@NLO	1.4069	29942	21.282
$t\bar{t}$	MC@NLO	87.419	139917	1.600
$W(\to \ell v) + $ (0-5) partons	ALPGEN	31799.178	5578612	0.175
$W(\to \ell v) + b\bar{b} + $ (0-3) partons	ALPGEN	9.516	16496	1.734
$Z(\to \ell\ell) + $ jets	ALPGEN	3099.288	1162916	0.375
Diboson ($WW+WZ+ZZ$)	HERWIG	16.159	749392	46.376
QCD (multijet + $b\bar{b}$)	ALPGEN	116633.100	1647992	0.014

Table 4.1: *List of MC samples used for the analysis: generators, cross sections, number of events and corresponding luminosity.*

Leading-Order event generator [45]. The hard process events can be completed by the initial and final state radiation, hadronization and decays, which are simulated with HERWIG 6.510. For the *t* and *s* channels, only the leptonic decay of the *W* bosons is considered (*e*, μ or τ). For the associated production (*Wt*), all the decay channels are considered. Therefore, the events that correspond to a fully hadronic (both *W* bosons decaying as $W \to q\bar{q}'$), dileptonic and semileptonic final states are all present in the signal sample. Following the discussion on subsection 2.3.1, in MC@NLO the intermediate $t\bar{t}$ state is removed using the Diagram Removal (DR) scheme. Here, one simply removes all diagrams in the NLO *Wt* amplitudes that are doubly resonant, where the intermediate $\bar{t}$ can be on-shell.

Top quark pair production was also generated with MC@NLO 3.4 . The fully hadronic final topology was not included in the sample. The events were hadronized with HERWIG and the underlying event was simulated by Jimmy 4.3 [46].

The background channels without top quarks (W + jets, Z + jets and W$b\bar{b}$ + jets) were generated using ALPGEN 2.13 Leading-Order Monte Carlo event generator [47] and hadronized with PYTHIA. Diboson events (WW, ZZ and WZ) were generated with HERWIG.

The QCD background was modeled using QCD multijet and QCD $b\bar{b}$ samples. These were generated using ALPGEN and HERWIG interfaced with Jimmy for parton showers. QCD background will be modeled using real data once it is available.

The Monte Carlo samples which were used for this analysis are described in Table 4.1. MC@NLO samples have event weights, where each event has a weight of either $+1$ or -1, and only the sum of the weights is a physical quantity.

4.2   Event Simulation and Reconstruction

The detector effects have to be considered and applied to the previously generated events. The simulation of the ATLAS detector can be performed using the full `GEANT4` simulation [48], where the reconstruction of the final state particles is based on the simulated signals on each ATLAS sub-detector. The full simulation takes into account the detailed interaction of each particle in the detector, allowing a realistic study of the performances of particle reconstruction and trigger. However, it is also very demanding in terms of the required computing time.

The signal and background events are passed through the complete `GEANT4` simulation of the ATLAS detector using version 15.6.3.10 of the ATLAS software `ATHENA` [49] to describe the geometry and response of the detector.

The objects in each event - electrons, jets, muons and missing transverse energy - are then reconstructed using `ATHENA 15.6.8.7` with the standard definitions and algorithms recommended and described by ATLAS [50].

Electrons

Electron candidates are reconstructed and identified in the calorimeters and in the inner detector, i.e., matching the electromagnetic energy deposits to the tracks. They are selected with a set of *medium* criteria, as defined in Ref. [51]. Only those in the range of pseudo-rapidity $|\eta| < 2.47$ and $p_T > 20$ GeV are reconstructed. However, electrons found in the crack region of the calorimeter ($1.37 < |\eta| < 1.52$) are discarded. An isolation criteria requires that the additional transverse energy E_T in a cone with radius $\Delta R = 0.2$ around the electron axis has to be less than $(4 + 0.023 E_T^{electron})$ GeV, where $E_T^{electron}$ is the transverse energy of the electron.

Jets

The reconstruction of the jets is based on the energy deposits in calorimeter towers, with a cone algorithm of radius $\Delta R = 0.4$. The transverse momentum of the jets is required to be greater than 20 GeV and the pseudo-rapidity in the range $|\eta| < 5.0$. Jet reconstruction algorithms provide a list of clustered calorimeter cells, which include both particle jet originated from electrons and from the decay of hadrons. Since some calorimeter clusters will be reconstructed as both electrons and jets, these last must be removed from the jet list in order to avoid double counting. Therefore, an overlap removal is made cutting on $\Delta R = \sqrt{\Delta\eta^2 + \Delta\phi^2}$. Those jets within $\Delta R < 0.2$ of a reconstructed electron are rejected.

Muons

Muons are reconstructed matching the muon spectrometer hits with the inner detector tracks. Muon candidates are require to have $p_T > 20$ GeV and $|\eta| < 2.5$. An isolation criteria similar to the one described for the electrons is applied for the muons: the transverse energy in a cone of $\Delta R = 0.2$ around the muon direction is required to be less than $0.1 p_T^{\mu}$, where p_T^{μ} is the transverse momentum of the muon. Also, the additional p_T in a cone of $\Delta R = 0.3$ must be less than 4 GeV. Finally, muons within a cone of radius $\Delta R < 0.3$ from a jet are removed, to reduce the selection of muons that arise from decays of hadrons inside jets. Here it is assumed that the energy released by the muons in the calorimeter does not give rise to reconstructed jets, so that no overlap removal between jets and muons rejecting the jet is applied.

Missing transverse energy

Missing transverse energy ($E\!\!\!/_T$) has two components: one that is associated with all stable and non-interacting particles in the final state, such as neutrinos; the other due to detector inefficiencies and resolution, which leads to the mismeasurement of the true E_T of the objects. The missing transverse energy $\vec{E\!\!\!/}_T$ is calculated as $-\sum_i E_T^i \hat{n}_i$, i.e., as the vector sum of the transverse energy deposits coming from the calorimeter cells, the measured muons and the energy losses in material in front of the calorimeter.

b-tagged jets

The ability to identify jets containing b-hadrons can be very useful for the data analysis. b-tagged jets are separated from jets coming from the hadronization of lighter quarks through some of their characteristic properties like their high mass and their relatively long lifetime of about 1.5 ps [52], which leads to a measurable flight of a few millimeters before their subsequent decay.

In the ATLAS detector, the b jets are tagged if they are in the range $|\eta| < 2.5$ and have $p_T > 15$ GeV [50]. The JetProb algorithm [53] was used for the b-tagging and set to an efficiency of 50%.

Chapter 5

Event Selection

The selection of events corresponding to the production of single top quarks in the semileptonic Wt-channel is described in this chapter. The event selection was developed in two parts: a sequential analysis and a discriminant analysis.

The analysis was performed for a luminosity of $\mathscr{L} = 200$ pb^{-1} and under the structure of the `LipCbrAnalysis` program [54, 55].

5.1   Single top Wt-channel

The signal for this analysis is the single top semileptonic Wt-channel.

In the first level of analysis (preselection) several cuts are made in order to have a sample of well reconstructed events and to reject most of the background that correspond to the other single top channels and to the major background processes: $t\bar{t}$, W + jets and QCD. These sequential cuts are based on the multiplicity, pseudo-rapidity and transverse momenta of the final state particles. The semileptonic single top Wt-channel final state topology is composed of one lepton ℓ, a b jet, two non-b jets (j_1 and j_2) and missing energy due to the neutrino, as shown in Figure 2.4. Since the lepton ℓ can be a τ lepton, and given its unstability, it should be noted that only its leptonic decays match this final state topology.

The aim of this selection is not only the rejection of background events but also the selection of the signal events for which a full reconstruction of the event kinematics is possible. The second level of analysis uses discriminant variables built from probability density functions to separate the signal from the background events.

43

5.1.1 Preselection

Sequential cuts are performed in order to select events matching the final state topology of the signal: $Wt \rightarrow \ell\nu bq\bar{q}'$. These cuts are the following:

1. Exactly 1 lepton with $p_T > 20$ GeV and $|\eta| < 2.5$ (in case of an electron $|\eta| < 2.47$ and excluding the crack region $1.37 < |\eta| < 1.52$) (see Figure 5.1);

2. Either 2, 3 or 4 jets (including b and non-b) with $p_T > 30$ GeV and $|\eta| < 5.0$ (Figure 5.2);

3. From the jets selected on the previous cut, at least 1 must be b-tagged (Figure 5.3);

4. $p_T^{missing} > 20$ GeV to be compatible with the presence of an escaped neutrino and high enough to avoid a low-energy region where fake $E_T^{missing}$ can be large (Figure 5.4).

5. At least 2 non-b jets between all the jets selected after the second cut. This will ensure that all the events can be used in the discriminant analysis and kinematics reconstruction (see Subsections 5.1.2 and 5.1.3).

In these cuts, variables such as the multiplicity of reconstructed objects in each event and their transverse momentum p_T are used. Some of the normalized distributions corresponding to these variables are shown in Figures 5.1 to 5.4 for signal and background events. The same normalized distributions are also shown after all the cuts have been applied.

After the presented preselection, only a certain number of signal and background events remain. These numbers are presented in Table 5.1, normalized to a luminosity of $\mathscr{L} = 0.200$ fb^{-1}. The signal efficiency ε, also shown, is defined as the ratio of signal events after and before the cuts.

It can be seen from Table 5.1 that the dominant background at this level is the $t\bar{t}$ process, representing $\sim 57\%$ of the total background. The $W+$ jets process is also important, contributing to about 30% of the background, while the other processes containing top quarks represent only 2%. It should be noted that the statistical error of the QCD samples is very large due to its large cross section and limited MC statistics. In the future, this process should be estimated using data-driven methods.

The signal to total background ratio achieved with this sequential analysis is only $\sim 4\%$. This means that to further eliminate background events, a discriminant analysis must be used. For example, a likelihood variable is more effective than the sequential cuts to discriminate signal from background events, since a likelihood uses the entire shape of several input variables.

Figure 5.1: *Normalized distributions of the multiplicity of leptons (top), the transverse momentum (middle) and pseudo-rapidity (bottom) of the lepton with highest p_T (on the left before the first cut and on the right after the last cut).*

Figure 5.2: *Normalized distributions of the multiplicity of jets (b + non-b) (top), the transverse momentum (middle) and pseudo-rapidity (bottom) of the jet with highest p_T (on the left before the second cut and on the right after the last cut).*
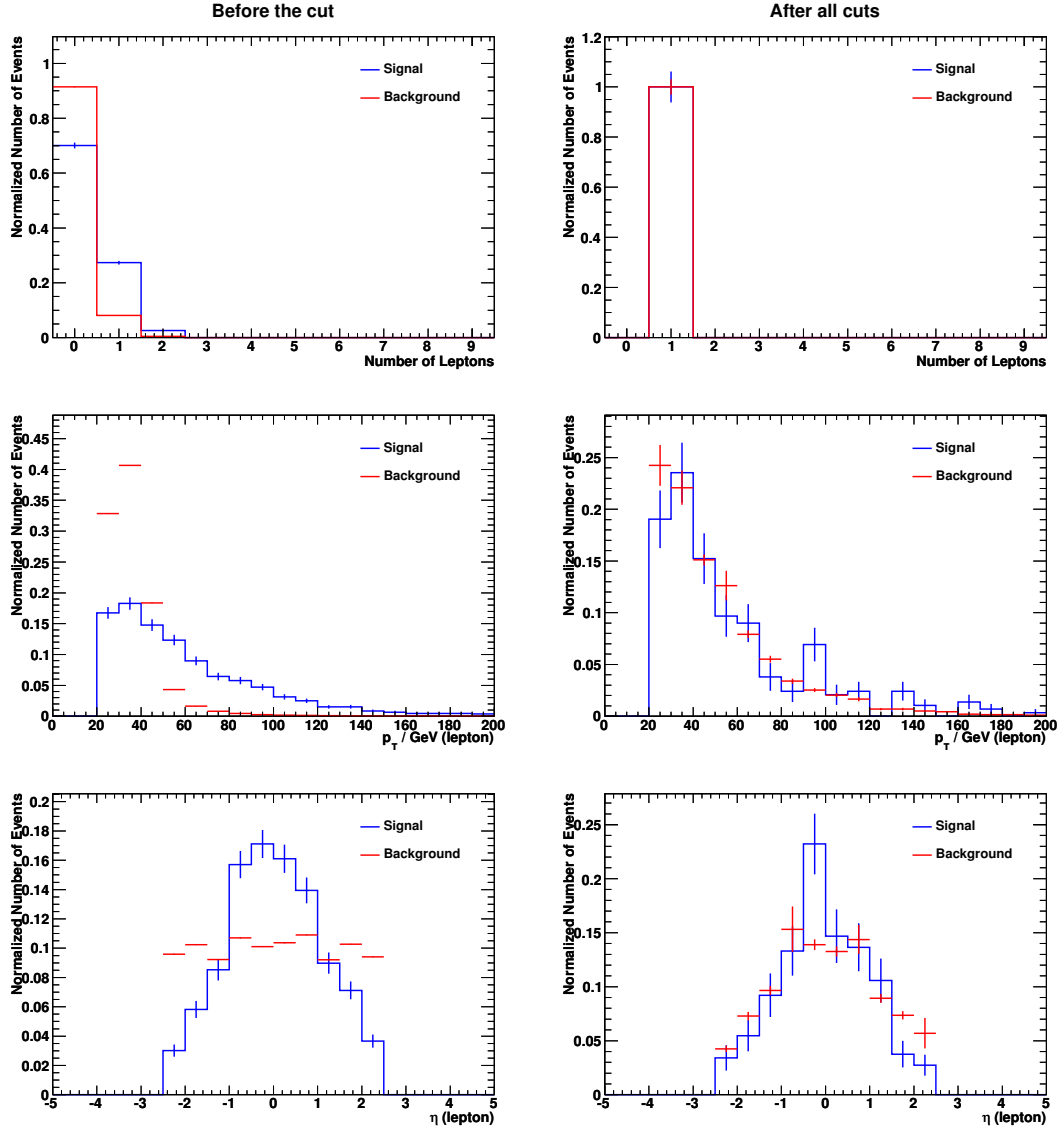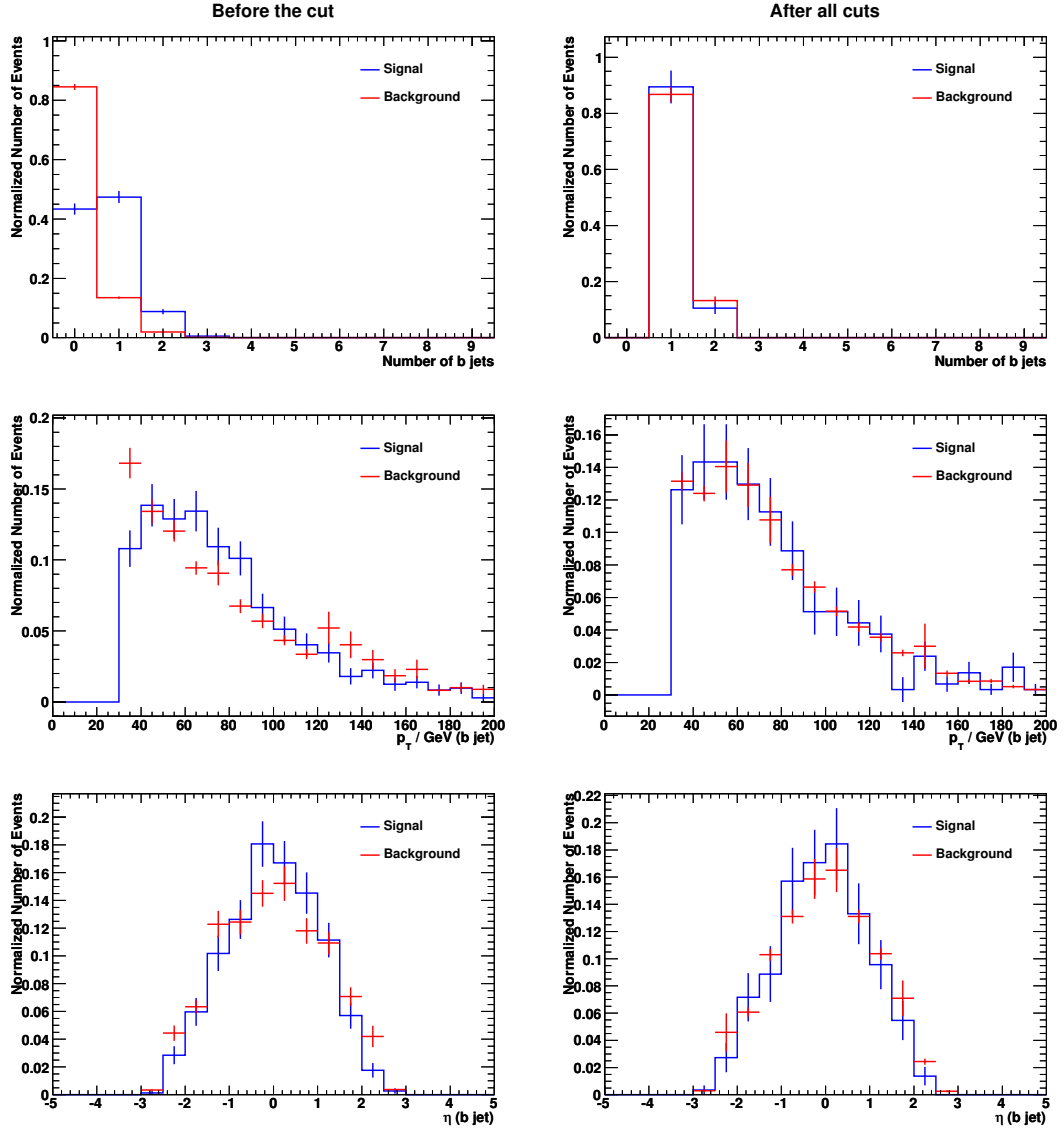
Figure 5.3: *Normalized distributions of the multiplicity of b jets (top), the transverse momentum (middle) and pseudo-rapidity (bottom) of the b jet with highest p_T (on the left before the third cut and on the right after the last cut).*
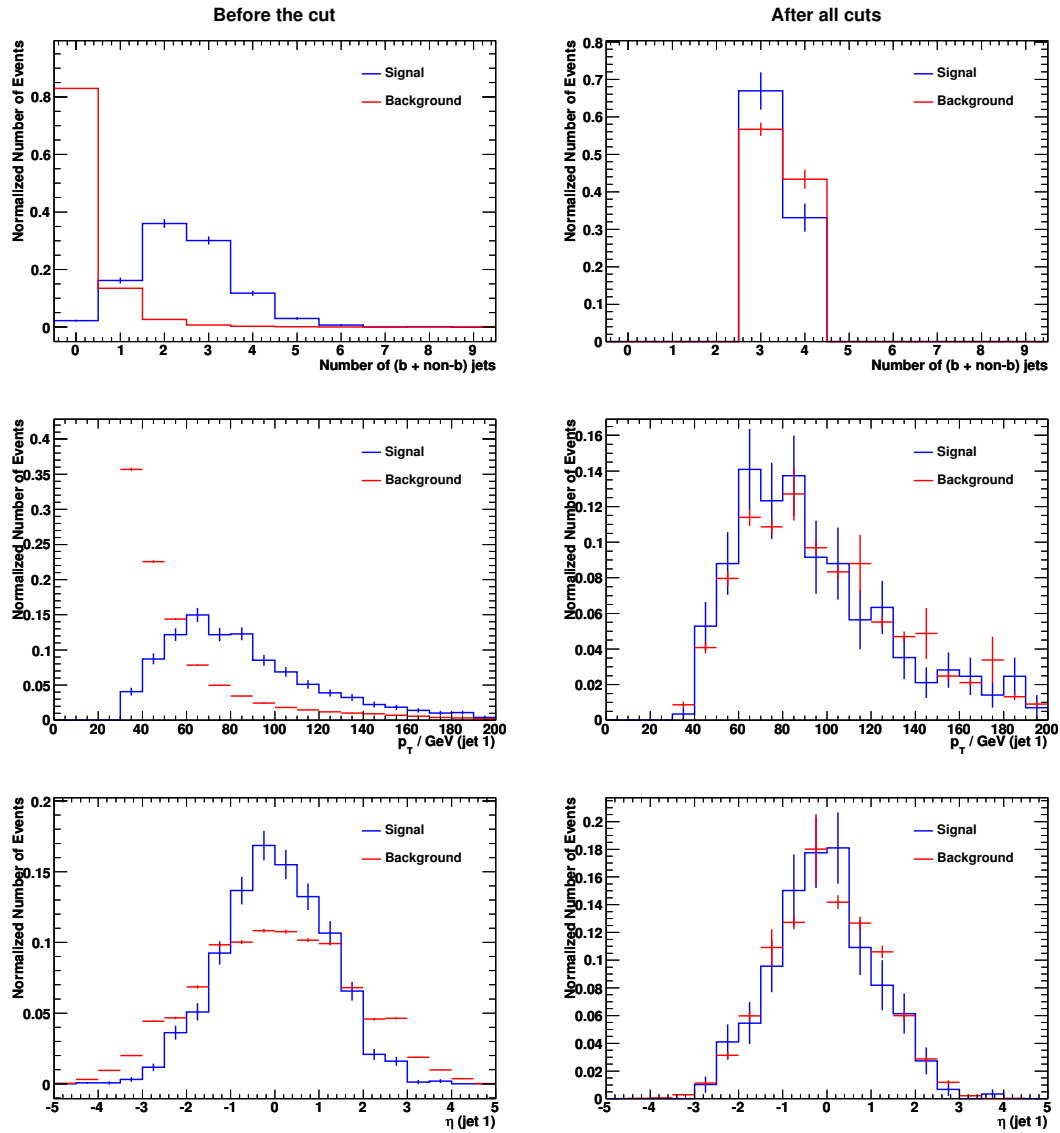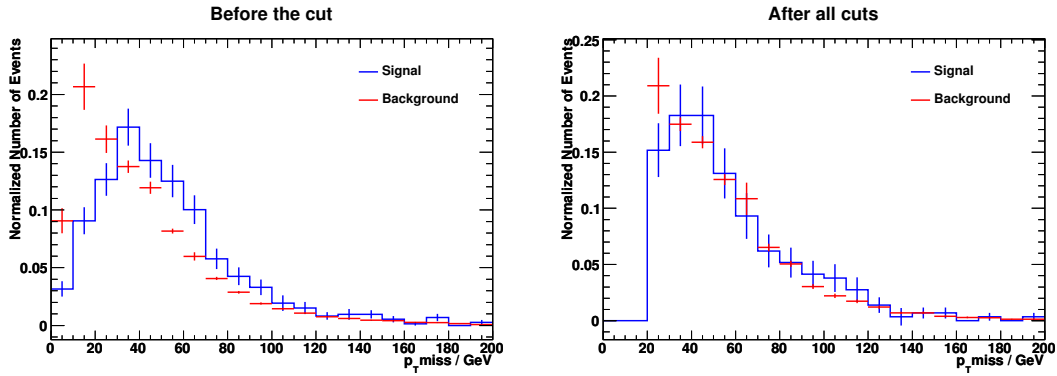
Figure 5.4: *Normalized distributions of the missing p_T (before and after the last cut).*

5.1.2 Discriminant Analysis

A set of variables was chosen to be used as probability density functions (p.d.f.). These should have different behaviours for signal and background, allowing for an efficient discrimination between the two types of events. A variable with high discriminating power results in a larger background rejection compared to the variation seen in the signal efficiency. The p.d.f.'s were built from the following 7 kinematical variables:

- the mass of the hadronic W boson, $M(W_{had}) = m_{j_1 j_2}$, where j_1 and j_2 are the two non-b jets with higher p_T;

- the pseudo-rapidity of the lepton;

- the transverse momentum of the b jet with higher p_T;

- the mass of the top quark reconstructed with the χ^2 method (see Section 5.1.3);

- the mass of the W from associated production reconstructed with the χ^2 method;

- the transverse mass of the leptonic W;

- the angle $\Delta\phi$ between the top quark and the W from associated production, both reconstructed with the χ^2 method.

These probability density functions are shown in Figure 5.5 after the preselection cuts.

Process	Events at preselection
Wt-channel	114.0 ± 6.3 ($\varepsilon = 4.38\pm0.24\%$)
t-channel	63.0 ± 3.7
s-channel	7.1 ± 0.3
$t\bar{t}$	1654.5 ± 18.0
W($\rightarrow \ell v$) + (0-5) partons	872.3 ± 29.5
W($\rightarrow \ell v$) + $b\bar{b}$ + (0-3) partons	52.3 ± 3.4
Z ($\rightarrow \ell\ell$) + (0-5) partons	82.5 ± 9.1
Diboson (WW+ZZ+WZ)	15.7 ± 0.5
QCD	163.7 ± 193.2
Total background	2911.1 ± 196.5
S/B	$3.92\,\%$
$S/\sqrt{S+B}$	2.07

Table 5.1: *Number of signal (S) and background (B) events after all preselection cuts, normalized to a luminosity of $\mathscr{L} = 0.200\,fb^{-1}$.*

Process	Events after final selection
Wt-channel	59.9 ± 4.7 ($\varepsilon = 2.22\pm0.17\%$)
t-channel	18.4 ± 1.9
s-channel	1.9 ± 0.2
$t\bar{t}$	571.5 ± 10.5
W($\rightarrow \ell v$) + (0-5) partons	212.6 ± 15.3
W($\rightarrow \ell v$) + $b\bar{b}$ + (0-3) partons	12.1 ± 1.6
Z ($\rightarrow \ell\ell$) + (0-5) partons	15.6 ± 5.0
Diboson (WW+ZZ+WZ)	4.9 ± 0.3
QCD	0.0 ± 193.2
Total background	837.0 ± 194.2
S/B	$7.16\,\%$
$S/\sqrt{S+B}$	2.00

Table 5.2: *Number of signal (S) and background (B) events after the final selection, normalized to a luminosity of $\mathscr{L} = 0.200\,fb^{-1}$.*

These p.d.f's allow the definition of signal and background likelihood variables, $\mathscr{L}_S$ and $\mathscr{L}_B$, respectively. For a given event, the likelihood of being of signal (background) type is obtained by multiplying the signal (background) probability densities of all input variables,
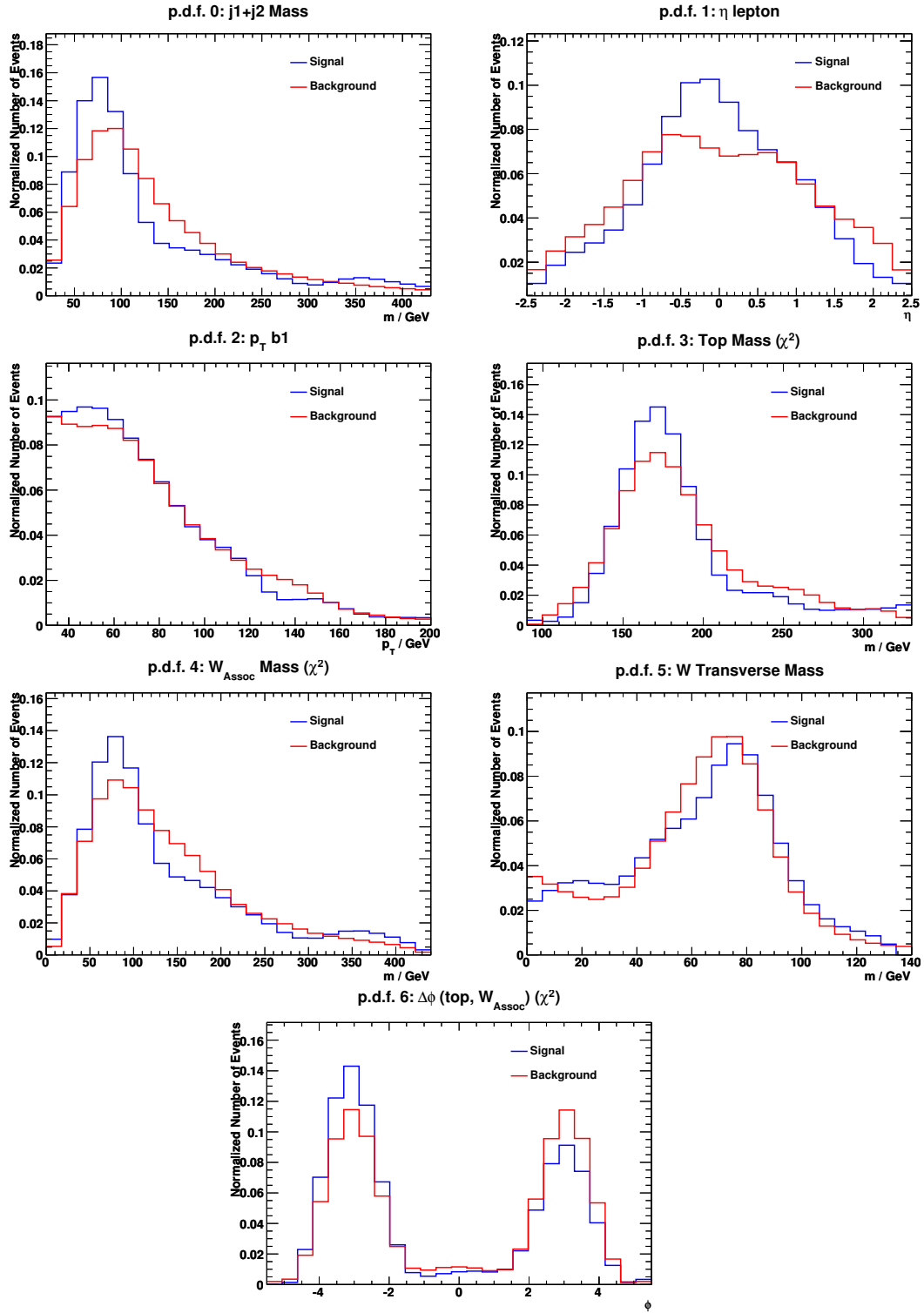
Figure 5.5: *Probability density functions for signal and background.*
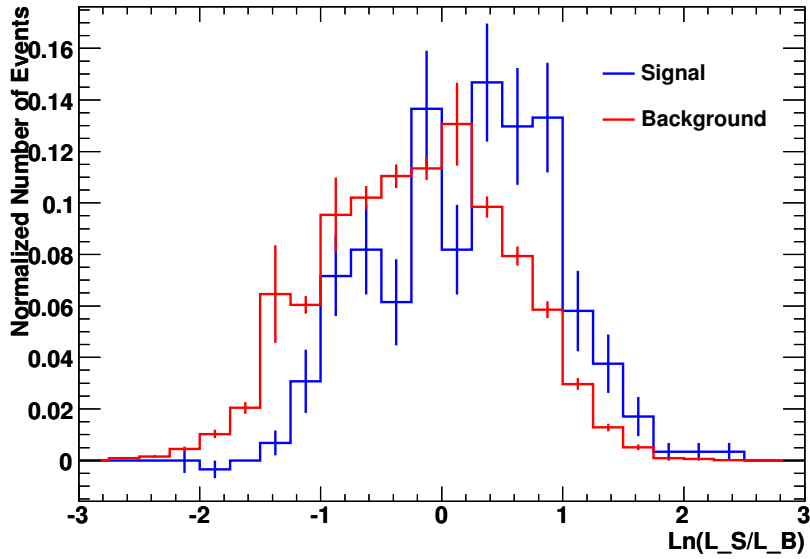
Figure 5.6: *Likelihood ratio for signal and background.*

which are assumed to be independent. A likelihood ratio $\mathscr{L}_R$ is built from these variables: $\mathscr{L}_R = \ln\left(\mathscr{L}_S/\mathscr{L}_B\right)$. The respective distribution is shown in Figure 5.6.

A cut on the likelihood variable can be made in order to achieve a higher signal to background ratio, without compromising the signal efficiency. Although this cut is not optimized, the $\mathscr{L}_R$ distributions obtained suggest the point $\mathscr{L}_R = 0.25$ as a minimum cut value to reject as much bakground as possible without losing too many signal events. The number of events that survive this last level of event selection ($\mathscr{L}_R > 0.25$) is presented in Table 5.2. The S/B ratio is maximized to about 7.2%.

Several other multivariate discriminators are available to optimize the discrimination against background events. The success of the various discriminant methods depends on the correlations between the 7 variables used. The likelihood discriminator ignores correlations among the variables, which can lead to a decrease of its performance.

5.1.3   Kinematics Reconstruction

For each event, the detector only provides information about the final state particles, meaning that the top quark and the other intermediate particles (like the two W bosons) have to be reconstructed from this information. The detector is expected to efficiently reconstruct two non-b tagged jets and missing transverse energy, to tag a b jet with a certain efficiency and to identify one charged lepton.

The neutrino is not detected, but the knowledge of its momentum is necessary to reconstruct the leptonic W boson. The other W boson (either coming from the associated production or the top quark decay) can be directly reconstructed from the two non-b jets. Assuming the missing transverse momentum in an event matches the transverse momentum of the neutrino, the conservation of energy and momentum on the W boson leptonic decay implies:

$$p^{\mu} p_{\mu} = m_W^2 = m_{\ell}^2 + 2E_{\ell}E_{\nu} + 2\vec{p}_{\ell} \cdot \vec{p}_{\nu} \approx 2E_{\ell}E_{\nu} + 2\vec{p}_{\ell} \cdot \vec{p}_{\nu}, \qquad (5.1)$$

and the z component of the neutrino momentum can be determined, using the on-shell mass of the W. Due to the resolution of the transverse missing energy, not all the events have a solution for the neutrino's longitudinal momentum. Moreover, if a solution exists, the complete final state can be reconstructed only up to a two-fold ambiguity, which results from the quadratic equation:

$$p_{\nu}^z = \frac{-b \pm \sqrt{b^2 - 4ac}}{2a}$$

$$a = (\frac{p_{\ell}^z}{p_{\ell}})^2 - 1$$

$$b = 2(\frac{p_{\ell}^x \not{p}^x + p_{\ell}^y \not{p}^y}{p_{\ell}} + \frac{m_W^2}{2p_{\ell}}) \frac{p_{\ell}^z}{p_{\ell}}$$

$$c = (\frac{p_{\ell}^x \not{p}^x + p_{\ell}^y \not{p}^y}{p_{\ell}} + \frac{m_W^2}{2p_{\ell}})^2 - \not{p}_T^2 \qquad (5.2)$$

where p_{ℓ}, p_{ℓ}^x, p_{ℓ}^y, p_{ℓ}^z are the charged lepton momentum and its components and $\not{p}_T$, $\not{p}^x$, $\not{p}^y$ are the missing transverse momentum and its components. In this analysis, when the quadratic equation 5.2 is used for the reconstruction, the chosen solution (when it exists) is the lowest in absolute value. After the determination of the neutrino momentum, the reconstruction of the leptonic W boson is possible.

The top quark is reconstructed associating the *b* jet with one of the *W* bosons. However, there are two *W* bosons, one originating from the top quark decay and the other from the associated production itself. To select the correct association between the *W* boson and the *b* jet for the reconstruction, three methods were tested.

First, using the quadratic equation to determine p_z^ν, a mass criteria selects the *bW* solution with an invariant mass closer to the top quark mass: 172.5 GeV. This reconstructs a top quark with either a leptonic or hadronic *W* (see in Figure 5.7 the events labeled as "Top Quark Lep" and "Top Quark Had" respectively).

Alternatively, the neutrino's longitudinal momentum component and the *W* boson plus *b* jet combination can be determined so that they minimize the expression:

$$\chi^2 = \frac{(m_{j_1 j_2} - m_W)^2}{\sigma_W^2} + \frac{(m_{\ell\nu} - m_W)^2}{\sigma_W^2} + \frac{(m_{bW_d} - m_t)^2}{\sigma_t^2}, \tag{5.3}$$

where the expected top quark and *W* boson masses and resolutions are $m_t = 172.5$ GeV, $m_W = 80.40$ GeV, $\sigma_t = 14$ GeV and $\sigma_W = 10$ GeV. The minimization of the χ^2 function depends on the p_z^ν value as well as on the correct pairing of the *W* boson to the *b* jet to reconstruct the top quark. The two hypothesis for the W_d boson (top quark decay product decaying to leptons or quarks) are tested and the solution corresponding to the minimum value of χ^2 is chosen for each event.

Since this method simultaneously approximates the value of p_z^ν to the top quark and *W* masses, it chooses preferentially the cases where the W_d boson decays leptonically. To correct for this effect, another method was implemented. The function to be minimized was defined as:

$$\Delta = |m_{l\nu} - m_W|, \tag{5.4}$$

depending only on the p_z^ν value. After the function Δ is minimized, the value of p_z^ν is used to reconstruct the leptonic *W*. The W_d boson is then determined as the one which leads to a top quark mass closer to 172.5 GeV.

It should be noted that these last two methods find p_z^ν solutions by minimization even for the events where the quadratic equation 5.2 doesn't have one. The distributions for the reconstructed masses of the top quark and the *W* bosons are shown in Figure 5.7 and 5.8, before and after the final selection.
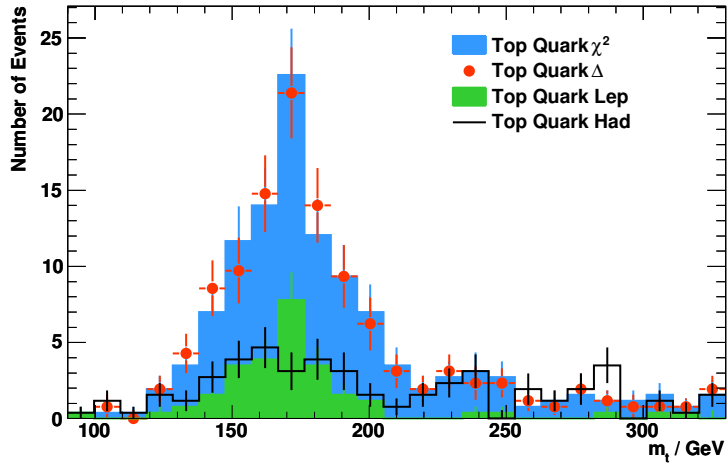
(a)
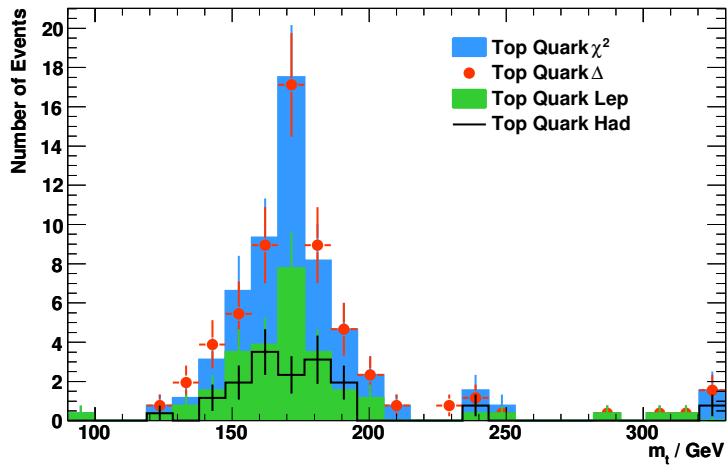
(b)

Figure 5.7: *Signal distributions of the mass of the top quark, according to different reconstruction methods (a) before and (b) after the final cut on the discriminant variable.*

(a)

(b)

Figure 5.8: *Signal distributions of the mass of the W bosons, according to two different reconstruction methods (a) before and (b) after the final cut on the discriminant variable.*

Chapter 6

Results

In this chapter, the estimate for the single top Wt-channel cross section and its statistical uncertainty are presented, for a centre-of-mass energy of 7 TeV and an integrated luminosity of 200 pb^{-1}.

6.1   Cross Section

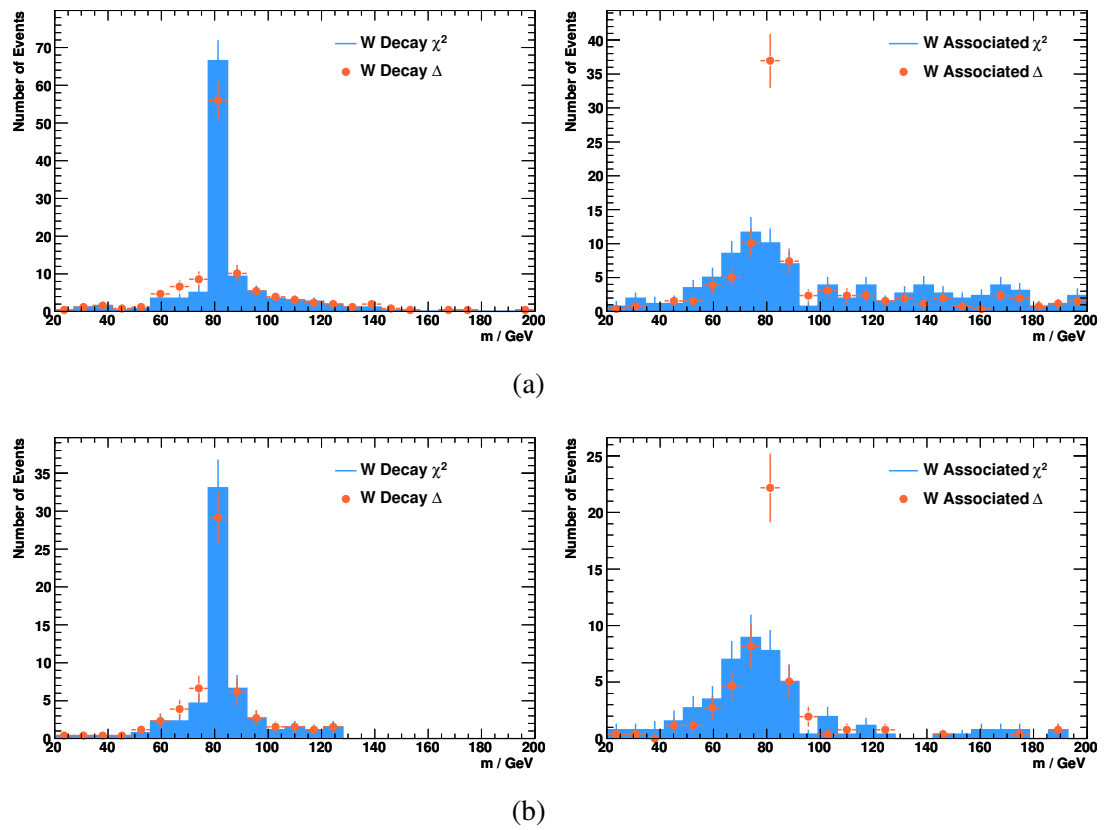To measure the cross section of the process in study, an estimate of signal events in a fake data sample must be measured. This calculation is done with two equivalent simulated samples assuming the SM: $D_1 = S_1 + B_1$ and $D_2 = S_2 + B_2$. However, D_2 is treated as fake data, which means there is no access to S_2 and B_2 separately, as in a real experimental result. Consequently, S_1 and B_1 are the reference samples on which the analysis presented in Chapter 5 was developed. An estimate of the number of signal events in the fake data sample D_2 is given by:

$$N = D_2 - B_1. \tag{6.1}$$

Experimentally, the number of observed events of a certain process is $N = \sigma \mathscr{L} \varepsilon$, where σ is the cross section of the process, $\mathscr{L}$ is the integrated luminosity and ε is the selection efficiency for signal events. This leads to an estimate of the single top Wt-channel cross section given by:

$$\sigma_{Wt} = \frac{D_2 - B_1}{\mathscr{L} \varepsilon_{Wt}}. \tag{6.2}$$

The cross section of the generated sample of Wt-channel events (including all the W decay channels) is 14.581 pb. The theoretical NLO value is 13.102 pb (see Section 2.3).

Signal efficiency

The signal efficiency can be obtained from the signal reference sample (S_1), dividing the number of events surviving the analysis cuts for the number of events in the generated sample. This corresponds to the following value, already shown in Table 5.2:

$$\varepsilon_{Wt} = \frac{S_1(\text{after selection cuts})}{S_1(\text{generator level})} = (2.22 \pm 0.17) \times 10^{-2}. \tag{6.3}$$

The geometrical acceptance of the detector, the trigger efficiency and the event selection efficiency all contribute to the efficiency ε_{Wt}.

Statistical uncertainties

The precision on σ_{Wt} depends on statistical and systematic errors, including the uncertainty on the measurement of the luminosity.

From equation 6.2, the statistical error associated with the determination of the cross section is given by:

$$\frac{\Delta\sigma_{Wt}}{\sigma_{Wt}} = \frac{\Delta N}{N} \oplus \frac{\Delta\varepsilon_{Wt}}{\varepsilon_{Wt}} \oplus \frac{\Delta\mathscr{L}}{\mathscr{L}}. \tag{6.4}$$

The systematic uncertainty of the luminosity measurement is estimated to be 11% (as can be seen on Figure 3.1) and to decrease as a function of time to about $\sim 5\%$.

The next step would be to include the sources of systematic uncertainty. There are detector-related uncertainties, such as those on particle identification efficiencies, on background rejections, on energy scales and resolutions, uncertainties that can be constrained and minimized with a better knowledge of the detector. These include the uncertainty on the Jet Energy Scale, on the *b*-tagging efficiency, the pile up effect, etc. There are also uncertainties coming from the approximations made in Monte Carlo generators and from theoretical uncertainties of the cross section calculations, in particular the scale dependence, the parton distribution functions and the experimental error on the top quark mass.

Result

The cross section of the Wt-channel is calculated at 7 TeV, considering an integrated luminosity of $\mathscr{L} = 0.200$ fb^{-1}. This result is presented in Table 6.1, considering only statistical uncertainties, which results in a precision of $\sim 82\%$. The obtained value is clearly dominated by the uncertainty on the number of QCD events.

Given the obtained result, and as a consequence of the background estimate precision, the luminosity error was not propagated into the overall calculation. Also, the determination of systematic uncertainties becomes important once the statistical uncertainty is controlled.

D_2	B_1	S/B	$S/\sqrt{S+B}$	Cross Section / pb	$\frac{\Delta\sigma}{\sigma}$
1079 ± 33	837.0 ± 194.2	7.2%	2.00	54.5 ± 44.6	81.8%

Table 6.1: *Number of events on the fake data and background reference samples, signal to background ratio and significance, measured cross section and precision, for a luminosity of $\mathscr{L} = 0.200$ fb^{-1} at $\sqrt{s} = 7$ TeV.*

This result stresses the importance of estimating major background contributions from data-driven methods, and not from MC simulation. During the early phases of LHC, studies based on MC to estimate the behavior of backgrounds such as QCD will not be reliable, making the use of data-driven methods imperative. In particular, a data-driven estimation is very important for the QCD multi-jet background: it is not possible to generate sufficient MC simulated QCD events, given the high QCD cross section. Furthermore, it suffers from large intrinsic uncertainties due to limited knowledge of the lepton fake rates and the total production cross section. A full quantitative evaluation of this background requires further study in data samples larger than those presently available.

Chapter 7

Conclusions

The ATLAS sensitivity to the cross section measurement of Wt-channel single top production at $\sqrt{s} = 7$ TeV was studied in the present thesis. The expected signal significance and the value of the Wt-channel production cross section were calculated for a luminosity of $200\,\mathrm{pb}^{-1}$, considering the semileptonic topology as signal. The cross section of this production channel has never been measured, since its contribution was very small at the Tevatron.

The full simulation of the ATLAS detector was used, allowing a detailed description of the detector geometry and reconstruction algorithms. The sequential and discriminant analyses developed to distinguish between signal and background events were presented. While the sequential analysis resulted in a signal to background ratio of only 4%, the discriminant analysis allowed a greater background elimination, reducing it by about 70% and maximizing the S/B ratio to $\sim 7\%$. The dominant background contributions correspond to $t\bar{t}$ and W+jets processes. Furthermore, making use of different methods, the reconstruction of the top quark and both W bosons was possible.

After maximizing the selection of signal events and the rejection of background events, the cross section value of the Wt-channel and its statistical uncertainty were estimated. With 200 pb^{-1}, the obtained result was $\sigma_{Wt} = 54.5 \pm 44.6\,\mathrm{pb}$, leading to a precision of $\frac{\Delta\sigma}{\sigma} = 82\%$.

Since large statistics will be achievable at the LHC, the systematic uncertainties are expected to be dominant. However, in this study the statistical errors have a very large contribution due to the limited statistics of the simulated QCD background. This inherent statistical uncertainty on Monte Carlo based QCD background estimates limits their use in early LHC running.

This analysis demonstrates the possibility of observing single top events on the Wt-channel with an integrated luminosity of 200 pb^{-1} and at 7 TeV at the LHC, provided

there is a reasonable background estimation. It is expected that in the early data analysis, backgrounds from $t\bar{t}$, W+jets and QCD production are not yet well understood. Therefore, to improve the signal to background ratios, an increase of statistics and the use of a data-based approach to estimate the backgrounds will allow the improvement of this result. Also, further multivariate analysis would be needed to isolate the signal.

The physics of the top quark will be one of the main physics topics at the LHC. The data from the ATLAS experiment at $\sqrt{s} = 7$ TeV will be crucial to its development. With a few tens of pb^{-1} the top quark rediscovery will be possible, through the pair production process. Then, a data sample of 100 pb^{-1} will suffice to observe single top quark production at the 4.2 standard deviation, considering the combined production of the t-channel and associated Wt production [56].

In conclusion, top quark physics is an active research area, due to the top quark interesting properties and because far less is known about it than about the other quarks and leptons. The top quark may lead to the discovery of new physics: its large mass may indicate a special role in electroweak symmetry breaking and evidence for particles yet unobserved may be revealed in its production or decay. Deviations from the SM may arise in decays for a charged Higgs boson, on anomalous couplings of the vertex Wtb, on an unexpected value of $|V_{tb}|$ indicating the existence of a heavy fourth generation, etc. The top quark study is then a potentially sensitive probe of new physics effects. On the other hand, its properties and production rates can be used in global electroweak precision fits to test the Standard Model and to constrain the mass of the elusive Higgs boson. Finally, it is also important to understand top quark events as much as possible because they will represent an important background contribution to many potential new physics signals in other searches.

Bibliography

[1] S. L. Glashow, *Partial Symmetries of Weak Interactions*, Nucl. Phys. 22 (1961) 579-588.

[2] S. Weinberg, *A Model of Leptons*, Phys. Rev. Lett. 19 (1967) 1264-1266.

[3] G. Zweig, *An SU(3) model for strong interaction symmetry and its breaking*, CERN-TH-401, 1964.

[4] C. Amsler *et al.* (Particle Data Group), Phys. Lett. B 667, 1 (2008).

[5] F. Halzen and A. D. Martin, *Quarks and Leptons: An Introductory Course in Modern Particle Physics*. New York, Usa: Wiley, 1984.

[6] K2K Collaboration, M. H. Ahn *et. al.*, *Indications of neutrino oscillation in a 250-km long baseline experiment*, Phys. Rev. Lett. 90 (2003) 041801.

[7] *The 2008 Nobel Prize in Physics - Press Release*, Nobelprize.org, http://nobelprize.org/nobel_prizes/physics/laureates/2008/press.html.

[8] The CKMfitter Group, J. Charles *et al.*, CP Violation and the CKM Matrix: Assessing the Impact of the Asymmetric B Factories, 2008, hep-ph/0406184.

[9] F. Abe *et al.*, *Observation of top quark production in $\bar{p}p$ collisions with the Collider Detector at Fermilab*, Phys. Rev. Lett. 74, 2626-2631 (1995).

[10] S. Abachi *et al.*, *Observation of the top quark*, Phys. Rev. Lett. 74, 2632– 2637 (1995).

[11] The Tevatron Electroweak Working Group for the CDF and D0 Collaborations, *Combination of CDF and D0 Results on the Mass of the Top Quark*, hep-ex/0903.2503v1.

[12] W. Wagner, *Top quark physics in hadron collisions*, Rep. Prog. Phys. 68 (2005) 2409-2494.

[13] W. Bernreuther, *Top Quark Physics at the LHC*, J. Phys. G 35 (2008) 083001.

[14] M. Cacciari, S. Frixione, M. M. Mangano, P. Nason and G. Ridolfi, *Updated predictions for the total production cross sections of top and of heavier quark pairs at the Tevatron and at the LHC*, JHEP 0809 (2008) 127.

[15] N. Kidonakis and R. Vogt, *The theoretical top quark cross section at the Tevatron and the LHC*, Phys. Rev. D 78 (2008) 074005.

[16] R. Bonciani, S. Catani, M. L. Mangano and P. Nason, *NLL resummation of the heavy-quark hadroproduction cross-section*, Nucl. Phys. B529 (1998) 424–450.

[17] J. Campbell, F. Tramontano, *Next-to-leading order corrections to Wt production and decay*, Nucl. Phys. B726 (2005) 109–130.

[18] Z. Sullivan, *Understanding single-top quark production and jets at hadron colliders*, Phys. Rev. D70 (2004) 114012.

[19] A. Shibata *et al.*, *Understanding Monte Carlo Generators for Top Physics*, ATL-COM-PHYS-2009-334.

[20] V. M. Abazov *et al.*, *Observation of single top-quark production*, Phys. Rev. Lett. 103 (2009) 092001.

[21] T. Aaltonen *et al.*, *First Observation of Electroweak Single Top Quark Production*, Phys. Rev. Lett. 103 (2009) 092002.

[22] The Tevatron Electroweak Working Group for the CDF and D0 Collaborations, *Combination of CDF and D0 Measurements of the Single Top Production Cross Section*, hep-ex/0908.2171v1.

[23] J. A. Aguilar-Saavedra, *Single top quark production at LHC with anomalous Wtb couplings*, 2008, hep-ph/0803.3810v3.

[24] J. A. Aguilar-Saavedra, J. Carvalho, Nuno Filipe Castro, Filipe Veloso, and A. Onofre, *Probing anomalous W t b couplings in top pair decays*, Eur. Phys. J. C50 (2007) 519-533.

[25] J. A. Aguilar-Saavedra, *A minimal set of top anomalous couplings*, 2008, hep-ph/0811.3842v2.

[26] G. Mahlon and S. J. Parke, *Single top quark production at the LHC: Understanding spin*, Phys. Lett. B 476 (2000) 323-330.

[27] Miguel Castro Nunes Fiolhais, *Study of ATLAS sensitivity to asymmetries in single top events*, CERN-THESIS-2009-014.

[28] G. Mahlon, *Spin Polarization in Single Top Events*, hep-ph/9811219v1.

[29] O. Bruning (Ed.) *et al*., *LHC design report. Vol. 1, 2, 3,* Tech. Rep. CERN-2004-003-V-1/2/3, 2004.

[30] The ATLAS Collaboration, *ATLAS Technical Proposal for a General-Purpose pp Experiment at the Large Hadron Collider at CERN*, CERN/LHCC/94-43 (1994).

[31] The CMS Collaboration, *CMS Technical Proposal*, CERN/LHCC/94-38 (1994).

[32] The ALICE Collaboration, *Technical Proposal for A Large Ion Collider Experiment at the CERN LHC*, CERN/LHCC/95-71 (1995).

[33] The LHCb Collaboration, *Technical Proposal: A Large Hadron Collider Beauty Experiment for Precision Measurements of CP Violation and Rare Decays*, CERN/LHCC/98-4 (1998).

[34] The TOTEM Collaboration, *Technical Proposal: Total Cross Section, Elastic Scattering and Diffraction Dissociation at the LHC*, CERN/LHCC/99-7 (1999).

[35] The LHCf Collaboration, *Technical Proposal for the CERN LHCf Experiment: Measurement of Photons and Neutral Pions in the Very Forward Region of LHC*, CERN-LHCC-2005-032, 2005.

[36] G. Aad *et al*., *The ATLAS Experiment at the CERN Large Hadron Collider*, JINST, 3:S08003, 2008.

[37] The ATLAS Collaboration, *Tile calorimeter technical design report*, CERN-LHCC-96-042, http://cdsweb.cern.ch/record/331062.

[38] M.C.N. Fiolhais and A. Onofre, *A more accurate description of noise in TileCal*, ATL-TILECAL-INT-2010-004.

[39] K. Kordas *et al*, *The ATLAS Data Acquisition and Trigger: concept, design and status*, Nucl. Phys. B 172 (2007) 178-182.

[40] R. W. L. Jones, *ATLAS computing and the GRID*, Nucl. Instr. Meth. Phys. Res. A 502 (2003) 372-375.

[41] J. C. Collins, D. E. Soper, *The Theorems of Perturbative QCD*, Ann. Rev. Nucl. Part. Sci. 37 (1987) 383.

[42] J. Pumplin *et al.*, *New Generation of Parton Distributions with Uncertainties from Global QCD Analysis*, MSU-HEP-011101, 2008.

[43] G. Corcella *et al.*, *HERWIG 6.5: An event generator for hadron emission reactions with interfering gluons (including supersymmetric processes)*, JHEP 0101 (2001) 010 [hep-ph/0011363].

[44] T. Sjostrand et. al., *PYTHIA 6.4: Physics and Manual*, hep-ph/0603175.

[45] S. Frixione and B. Webber, *The MC@NLO 3.4 Event Generator*, hep-ph/0812.0770v1.

[46] J. M. Butterworth, J. R. Forshaw and M. H. Seymour, *Multiparton interactions in photoproduction at HERA*, Z. Phys. C72 (1996) 637–646.

[47] M. L. Mangano, M. Moretti, F. Piccinini, R. Pittau, A. Polosa, *ALPGEN, a generator for hard multiparton processes in hadronic collisions*, JHEP 0307:001, 2003, hep-ph/0206293.

[48] GEANT4 Collaboration, S. Agostinelli *et al.*, *GEANT4 - a simulation toolkit*, Nuc. Instr. Meth. Phys. Res. A 506 (2003) 250-303.

[49] The ATLAS Collaboration, *The ATLAS Computing Workbook* (`ATHENA 15.6.3.10`), Webpage available in https://twiki.cern.ch/twiki/bin/view/Atlas/WorkBook.

[50] The ATLAS Collaboration, *Expected Performance of the ATLAS Experiment - Detector, Trigger and Physics*, CERN-OPEN-2008-020.

[51] The ATLAS Collaboration, *Observation of $W \rightarrow \ell\nu$ and $Z \rightarrow \ell\ell$ production in proton-proton collisions at $\sqrt{s} = 7$ TeV with the ATLAS detector*, ATLAS-CONF-2010-044.

[52] T. Gopfert, *Tagging b-jets in ATLAS,* ATL-PHYS-PROC-2010-014.

[53] The ATLAS Collaboration, *First look at the JetProb b-tagging algorithm in the 900 GeV collision data with the ATLAS detector*, ATLAS-CONF-2010-010.

[54] Nuno Filipe da Silva Fernandes de Castro, *Study of the Wtb vertex structure at the ATLAS experiment*, CERN-THESIS-2008-083.

[55] Filipe Manuel Almeida Veloso, *Study of ATLAS sensitivity to FCNC top quark decays*, CERN-THESIS-2008-106.

[56] J. L. Holzbauer, P. Ryan, B. G. Pope, R. Schwienhorst, *Prospects for single top quark observation with ATLAS data at 10 TeV and at 7 TeV*, ATL-COM-PHYS-2010-324.